AN ABSTRACT OF THE THESIS OF

Christine M. Greiser for the degree of Master of Science in Atmospheric Sciences presented on January 25, 2002

Title: Surface Heat Flux Estimates from NCAR Electra Data Over the Pacific Warm Pool During TOGA COARE

Abstract Approved: Redacted for Privacy

The warm pool region of the western tropical Pacific is of particular interest to atmospheric dynamics because it represents a significant source of energy to the atmosphere. A better understanding of heat transfer driven by mesoscale and turbulent circulations within this region could lead to improved global circulation models, and therefore to improved prediction of global weather patterns. A first step to this understanding is to evaluate empirical data as well as the methods used to estimate heat transfer, or heat flux, at the surface. Of specific interest here are latent heat flux, the heat transfer associated with evaporation, and sensible heat flux, the heat transfer associated with convection and conduction. In this paper, two different methods of turbulent flux calculation, eddy correlation and the bulk aerodynamic method are compared. Eddy correlation directly uses turbulence measurements to estimate heat flux whereas the bulk aerodynamic method relies on similarity theory to relate heat flux to mean flow quantities. A brief discussion of selection of averaging length based on flight altitude is included, as well as a comparison of errors introduced in averaging velocity as a scalar or as a vector. Errors introduced by averaging, including mesoscale flux enhancement, are evaluated for strong and weak wind cases

during relatively light convection in the region. Finally, month to month variability in heat flux is evaluated in an effort to further understand the accuracy of various approximations used in flux calculation.

Surface Heat Flux Estimates from NCAR Electra Data Over the Pacific Warm Pool During TOGA COARE

by

Christine M. Greiser

A THESIS

submitted to

Oregon State University

in partial fulfillment of
the requirements for the
degree of

Master of Science

Presented January 25, 2002
Commencement June 2002

Master of Science thesis of Christine M. Greiser presented on January 25, 2002.

APPROVED:

Redacted for Privacy

Major Professor, representing Atmospheric Sciences

Redacted for Privacy

Dean of College of Oceanic and Atmospheric Sciences

Redacted for Privacy

Dean of Graduate School

I understand that my thesis will become part of the permanent collection of Oregon State University libraries. My signature below authorizes release of my thesis to any reader upon request.

Redacted for privacy

Christine M. Greiser, Author

ACKNOWLEDGMENTS

The author would like to thank Steven Esbensen, Irma Delson, and Dean Vickers at Oregon State University for their support in completion of the work. Special thanks to Mel Greiser for his encouragement and support throughout the project. Work for this thesis was supported by the National Science Foundation under grant ATM-9313588.

TABLE OF CONTENTS

TABLE OF CONTENTS (CONTINUED)

LIST OF FIGURES

LIST OF FIGURES (CONTINUED)

LIST OF TABLES

Surface Heat Flux Estimates from NCAR Electra Data Over the Pacific Warm Pool During TOGA COARE

1. Introduction

The TOGA Coupled Atmosphere-Ocean Research Experiment (COARE) took place in the Western Tropical Pacific warm pool region during 1992 and 1993. The underlying premise of TOGA is that the ocean and atmosphere act as a coupled system, communicating through the effects of surface wind stress and the surface heat and water fluxes. Its objectives (as outlined in the TOGA planning document, WMO 1985) include describing the tropical ocean and global atmosphere in time with the ultimate goal of understanding and describing its predictability. It also investigated the feasibility of modeling the coupled ocean-atmosphere system. Improved parameterization of air-sea fluxes, planetary boundary layer processes, and oceanic mixed layer properties are crucial to the success of the modeling efforts.

Within the context of TOGA, COARE had four stated objectives. Specifically laid out in Webster and Lukas (1992), these objectives were:

> To describe and understand (1) the principal processes responsible for the coupling of the ocean and atmosphere in the western Pacific warm pool system; (2) the principal atmospheric processes that organize convection in the warm pool region; (3) the oceanic response to combined buoyancy and wind stress forcing in the western Pacific warm pool region; (4) the multiple scale interactions that extend the oceanic and atmospheric influence of the western Pacific warm pool system to other regions and vice versa.

The focus on the warm pool region is desirable because it represents the main source of energy (in the form of rainfall and latent heat release) on the planet. A solid understanding of atmospheric and oceanic physical processes in this region is crucial to accurate global climate modeling and prediction.

This paper addresses first the goal of understanding the processes responsible for ocean-atmosphere coupling by examining bulk sensible and latent heat flux estimates under "light" (<4 m/s) and "strong" (>4 m/s) wind conditions. Second, a contribution is made to the effort to improve parameterization of mesoscale heat flux by attempting to understand the magnitude of mesoscale flux enhancement during the intensive observation period and by evaluating wind speed effects in buoyancy-driven (weak wind) conditions.

1.1 Review of past work

One source of error in global circulation models in the contributions of large eddy and mesoscale motions, that is, motions on the order of 1 km to 5 km in size, to the energy budget. For reference, grid sizes used in global climate modeling can be on the order of 100 km. Because of the relatively coarse resolution in these models, the smaller-scale motions (i.e., turbulent, convective, and mesoscale motions) are not explicitly represented. This means that the effects of either deep convection or of boundary layer free convection can contribute to the total heat flux and should be parameterized appropriately (Redelsperger, 1999). Redelsperger (1999) parameterizes these effects in terms of a "gustiness" parameter. Observations show that such variations in wind speed and direction can have an effect on the computed surface heat flux (Esbensen and McPhaden (1996) and Hasse and Smith (1997), for example). On overview of gustiness as it applies to the COARE algorithm is presented in chapter 4. Godfrey and Beljaars (1991), Ledvina et al. (1993), Mahrt and Sun (1995), Esbensen and McPhaden (1996) and Vickers and Esbensen (1998) all look to evaluate the effect of gustiness on surface heat flux (i.e., mesoscale flux enhancement) by distinguishing

between vector-averaged and scalar-averaged wind speeds. This approach is taken for several TOGA COARE Electra flights in chapter 5 of this paper.

A more basic issue in flux parameterization is the algorithm used to arrive at the heat flux estimate. The COARE algorithm has been explained and evaluated frequently in the literature. For example, Fairall et al. (1996) explain the formulation of the algorithm and Zeng et al. (1998) and Chang and Grossman (1999) compare it to several other parameterizations. Kara et al. (2000) explain the computational cost benefit of such a simple, if accurate, model. An overview of the bulk algorithm used in this paper is given in Chapter 4 and a comparison to eddy correlation results is presented in Chapters 5 and 6.

Critical to the successful interpretation of an eddy correlation flux calculation is selection of a proper averaging length. Averaging lengths that are too long can result in errors due to inclusion of mesoscale motions and too short can result in errors due to inadequate sampling of turbulent elements. The conventional method of choosing averaging length has been based on turbulence cospectra and is reviewed extensively in the literature (Lenschow et al. (1994), Sun et al. (1996), and Friehe et al. (1991), for example). Briefly, the method involves computation of ogives by integration of the turbulence cospectra. The resulting ogive is a relatively smooth curve, which represents cumulative flux as a function of wavelength (or averaging length as applied in this paper) and which reaches a constant value at low frequencies, indicating that all of the flux has been captured. Williams and Hacker (1995), Williams et al. (1996) and Rogers et al. (1995) apply this method to aircraft data with good results as well. Chapter 3 reviews, in depth, the selection of appropriate averaging length scales for this study.

1.2 Scope of current research

Surface fluxes in homogeneous conditions have been studied fairly extensively (Garratt (1977), Smith (1988), Sun and Mahrt (1995), Stull (1988), Garratt (1992)) and

the bulk aerodynamic method has become a standard method for flux estimation (Esbensen and Reynolds (1981), Sun et al (1996)). Problems arise, however in applying bulk aerodynamic theory over inhomogeneous areas. Over the ocean, inhomogeneity in surface fluxes is introduced by sporadic mesoscale systems that are not tied to any specific surface feature. Mahrt and Sun (1995) review several approaches for dealing with inhomogeneity. They assert that although the flow at the surface may not achieve equilibrium over any given patch of surface, flow higher up does achieve equilibrium. They further assert that above this "blending height" the fluxes become horizontally invariant and can be related to "effective" surface properties. They investigate three approaches for dealing with surface heterogeneity including correcting the grid-averaged flux via use of a spatial Reynolds term parameterizing subgrid variations in the flux. Chapter 5 investigates one aspect of the Reynolds term parameterization, mesoscale enhancement of surface heat flux. This is important because current global circulation models have resolution that tends to be more coarse than the scale of many mesoscale systems which implies inclusion of mesoscale transport in turbulent flux parameterizations may be important. This issue is explored further in section 5.2 and the results discussed here are compared to work by Esbensen and McPhaden (1996) and Vickers and Esbensen (1998).

In determining the appropriate averaging length to isolate the fluxes due to turbulent motions, several approaches have been taken. Section 3.1 investigates one of these approaches and the impact of altitude on the proper averaging length. In choosing a local averaging length, Sun et al (1996) use the method outlined in section 3.1 which was developed by Howell (1995) and is similar to spectral analysis. This approach allows choice of a local averaging length using local basis functions, rather than the "global" basis functions of Fourier analysis. Spectral analysis using Fourier basis functions by Williams et al. (1996) leads them to choose a local averaging length slightly different in magnitude. Again, the problem is further complicated in global circulation models (GCM) by virtue of the grid size. Because the grid is larger than the local flux averaging scale (FAS), the fluxes must be averaged a second time. Mahrt

(1987) and Lenschow et al. (1994) have investigated this problem. Efforts have been made to determine not only separation lengths between turbulent and mesoscale transport, but also to understand the implications of including mesoscale quantities in turbulent flux calculations (Sun et al. (1996), Esbensen and McPhaden, (1996), Esbensen and Reynolds (1981)). Estimates of mesoscale enhancement of heat flux analogous to those in Esbensen and McPhaden (1996) but using aircraft data are reviewed in this paper.

Chapter 2 discusses the data selected for use in this study as well as methods used to complete measurements during TOGA COARE. This is followed in Chapter 3 by a brief explanation of the eddy correlation method for computing surface heat flux and a discussion of how averaging lengths have been selected. There is a brief overview of the bulk aerodynamic method of flux calculation included in Chapter 4. Chapter 5 offers a comparison of TOGA COARE heat flux estimates using direct and bulk methods and some discussion of mesoscale enhancement of surface flux. Finally, flux trends from month to month are examined in Chapter 6 of this paper.

1.3 Relevant conclusions

The thrust of this paper is to explore the relationship between bulk and eddy correlation fluxes in convectively-driven boundary layers. Even with judicious selection of local averaging lengths, and using a state-of-the-art bulk flux algorithm, the bulk aerodynamic method still tends to over-predict aircraft heat fluxes in the TOGA COARE region. The bulk aerodynamic method is not valid outside of the surface layer, so, as expected, the error between bulk and eddy correlation heat fluxes increases with increasing altitude for both evaporation (latent heat flux) and sensible heat flux. A surprising result is that this bias persists even within the surface layer (below 100m). Possible causes include errors in Monin-Obhukov similarity profiles within the surface layer (which is about 10 m in the TOGA COARE domain, Vickers and Esbensen (1998)) and errors in ambient and sea-surface temperature measurement. Relevant

corrections included in the COARE bulk algorithm (e.g., the gustiness correction) are briefly discussed in this context in Chapter 4.

A review of eddy correlation flux calculation is presented in Chapter 3, along with a discussion of one method for choosing the averaging length in flux calculation. The main assertion there is that the proper choice of the averaging length scale used in eddy correlation flux calculation is crucial to isolating the effects of turbulent motions while excluding larger-scale transport processes. It will be shown that the appropriate averaging length scale increases with altitude from 1 km near the surface to 3 km above 250 m.

Next, the bulk aerodynamic method and COARE algorithm are introduced and discussed (Chapter 4). Bulk and eddy fluxes computed from the TOGA COARE data are then compared in Chapter 5. It will be shown that there is a significant bias between the two flux calculation methods at altitudes above the surface layer and that this bias persists even below 100m. It is not until below ~30 to 50 m that bulk estimates reasonably predict eddy fluxes. Mesoscale enhancement of flux is discussed in Chapter 5 as well. Specifically, it will be shown that mesoscale enhancement increases as wind speed decreases and that this effect is more significant for sensible heat flux calculations. These differences are broken down month by month and are discussed further in Chapter 6.

2. Data Selection and Humidity Measurement

An overview of data selected for this study and the instrumentation used aboard the Electra is presented in this chapter. The first section briefly describes instrumentation requirements for both eddy correlation flux calculation and flux estimation by the bulk aerodynamic method. The discussion of specific instrumentation is then paused for a brief overview of flight selection criteria (section 2.2). We return to the discussion of instrumentation with a brief overview instrumentation relevant to flux calculation section 3, followed by an in depth discussion of humidity measurement and its calibration in section 4.

2.1 Data requirements for flux calculation

Eddy correlation flux calculation involves products of fast response (20 Hz during TOGA COARE) perturbations of two time series from their local means. For example, a time series may be separated into two parts as follows:

$$\phi'(t) = \phi(t) - \overline{\phi}$$

where the overbar indicates a local average value and the prime is the perturbation from that local mean. A more specific description of eddy correlation flux calculation is given in chapter 3. Direct calculation of the flux requires fast response measurements of temperature and vertical wind speed for sensible heat flux and measurements of humidity and vertical windspeed for latent heat flux.

In contrast, estimation of the surface heat flux by the bulk aerodynamic method uses similarity relationships to estimate surface heat flux from mean meteorological values. In this case, then, it is reasonable to use slow response data. (1 Hz during TOGA COARE). An overview of the bulk aerodynamic method for flux calculation method is presented in chapter 4. This method requires that more parameters are measured (e.g., radiometric surface temperature, ambient temperature,

altitude, mixing ratio, horizontal wind speed, and air density) or calculated (e.g., surface mixing ratio, air density).

2.2 Selected flights

The availability of TOGA COARE aircraft data taken at several altitudes within the boundary layer provides a unique opportunity to evaluate the dependence of locally averaged fluxes on changes in altitude. By choosing a single local averaging scale and calculating the bulk and eddy correlation fluxes at several altitudes, it is possible to gain some insight into the performance of the Monin-Obhukov similarity theory over a range of scales. Consequently, one may make a statement about the ability of the bulk method to predict the fluxes over a range of altitudes and the necessity to vary the local averaging scale over these altitudes.

The data selected for this study consists of 168 level flight legs, flown by the NCAR Electra during the months of November 1992, December 1992, and January 1993. "Level flight legs" include those flights with altitude change of less than 100m over the entire leg. This eliminates the possibility of rapid changes in the slow response vapor density information and therefore ensured the least suspect set of fast response data. Lengths of the legs range from a minimum of 20 km up to 157 km, covering an average distance of 60 km. The minimum length constraint was chosen in order to avoid sampling errors within the leg. Average flight altitudes range from 29 m to 989 m (with a median altitude of 63 m) and wind speeds on the flights range from 0 m/s to slightly less than 10 m/s (median wind speed is 3.1 m/s).

2.3 Instrumentation used on the NCAR Electra during TOGA COARE

Wind components on the Electra were measured using a gust probe, which consists of a pitot probe for static pressure measurement, angle of attack, and sideslip angle vanes. Data was corrected with reference to GPS information. Temperature at the aircraft altitude was measured at the same location as the gust probe with a Rosemount resistance thermometer. Radiometric sea surface temperature was

measured using a Barnes PRT4 radiometer, calibrated during flight. More information on the specifications of the instrumentation used may be found in Grant and Hignett (1996).

Humidity was measured from the Electra using three separate instruments - low frequency humidity response was measured using a dewpoint hygrometer, while high frequency data was recorded with both a Lyman-alpha hygrometer and an experimental UV hygrometer. Accurate fast-response measurement of humidity is difficult, as the Lyman-alpha instrument is known to drift. During TOGA COARE, in-situ calibration was performed by coupling the fast-response instrument to the more reliable chilled mirror instrument. Specifics of these instruments, as well as a comparison of two methods of calibrating the resulting data follow in the next section.

2.4 Humidity measurement

2.4.1 Instrumentation

In calculating turbulent water vapor flux, it is necessary to have access to high frequency vapor density information. The Lyman-alpha hygrometer is capable of measuring this high frequency vapor density from aircraft platforms like the NCAR Electra flown during TOGA COARE. The instrument, however, has been noted to drift from its calibration and cannot be used independently (Schanot, (1987)). This drift has led to the practice of comparing the output of the Lyman-alpha hygrometer to a more widely trusted slow response humidity instrument, in this case, the EG&G dewpoint hygrometer. Several methods exist to calibrate the Lyman-alpha to the EG&G. This section explores the differences between two methods, loose coupling of the Lyman-alpha response to the dewpoint hygrometer output (used by NCAR; i.e., the `NCAR Method') and a linear calibration method presented by Friehe et al. (1986) (i.e., the `FGP Method').

Of the sixty-eight TOGA COARE Electra flight legs evaluated which met the flatness and length criteria previously outlined, twenty-five were from flights RF20,

RF2l, and RF22 and were used for the initial analysis. The remaining forty-three, from flights RF23 through RF32, were used as an independent check to ensure correctness of the results (see section 2.2.6). Visual inspection of the legs showed that the trends of the EG&G and Lyman-alpha data were drastically different for one leg of RF20. The data for this leg is considered suspect, and will not be analyzed further in this paper. A comparison between the Lyman-alpha and experimental UV hygrometer was performed using data from flights RF20 and RF2l, the only flights during which both instruments simultaneously appeared to be working well.

2.4.2 Calibration by the loose couple technique

The loose couple technique used by NCAR is based on the premise that the Lyman-alpha may be calibrated in the lab to derive an empirical calibration curve. It asserts that the slope of the water vapor density calibration curve does not change with time, but has a time dependent bias, shifting the curve up and down relative to voltage (Figure 2.1). To remove the bias error, the NCAR methods couples the low frequency Lyman-alpha response to the mean humidity data, provided by the EG&G chilled mirror instrument (NCAR personal communication and Schanot, (1987)). A step by step procedure follows.

A third-order curve-fit of the Lyman-alpha response is empirically determined in advance by comparison with a known standard. An estimate of the Lyman-alpha absolute humidity (ρ_L) is calculated from the uncorrected chilled mirror instrument response using the empirically derived curve. The difference between ρ_L and the concurrent slow response value (ρ_{CM}) is determined for each one-second interval and a correction factor is calculated. A fraction of the correction factor is then applied to the Lyman-alpha signal at each time step within the one-second interval, tending to gradually reduce the difference between ρ_L and ρ_{CM}. The corrected Lyman-alpha vapor density is finally calculated using the same empirical Lyman-alpha response curve referenced before and the corrected voltage. It is in this way that the mean

Lyman-alpha baseline is forced toward the slow-response vapor density measured by the chilled mirror (Schanot, 1987).

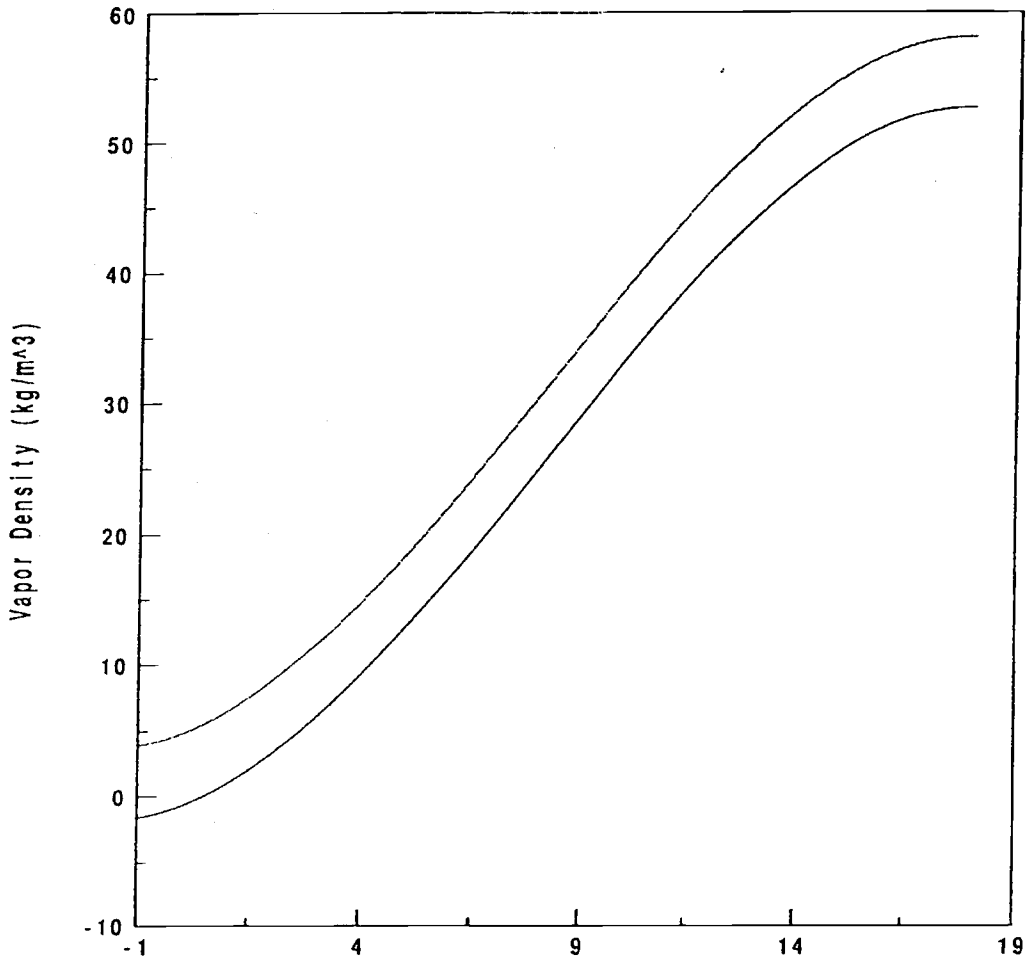

Figure 2.1: RAF empirical curve

2.4.3 Calibration by the FGP method

The method proposed by Friehe et al. (1986) provides a linear calibration between the EG&G slow response water vapor density and the low frequency portion of the Lyman-alpha signal for a. level flight leg. It is based on the idea that there exists

a linear relationship between the voltage response of the Lyman-alpha and the true water vapor density over a limited range of humidities. Where the NCAR method leaves the high frequency portion of the data untouched, the FGP method universally applies a correction to both the high frequency and low frequency portions of the Lyman-alpha signal. Again, the fast response signal is calibrated to a known mean value, but the procedure for obtaining the corrected vapor density is different.

The time series from the Lyman-alpha and the chilled-mirror instrument are correlated to find the time lag inherent to the response of the chilled-mirror instrument. The chilled-mirror data series is advanced by the time lag and is then low pass filtered. Likewise, the Lyman-alpha time series is low-pass filtered. Using a regression analysis, a linear relationship between the two low-pass filtered series is determined. The resulting slope and intercept represent the calibration curve applicable to this particular flight leg. The linear calibration curve is applied to the original Lyman-alpha time series to calculate the corrected fast-response vapor density (Friehe et al., 1986).

2.4.4 Comparison procedure

To determine specific differences between the NCAR and FGP methods, a matrix of similarity is constructed in which the original signal is broken down into high frequency and low frequency parts by means of a linear filter. Figure 2.2 shows the controlling factor determining the calibration curve for each portion of the frequency domain. Note that the shape of the response curve for each space in the matrix is determined by only one instrument (i.e., the chilled mirror instrument or the Lyman-alpha). This working hypothesis is confirmed statistically using regression analysis.

Figure 2.2 provides the framework for the comparison of the NCAR Method and the FGP method. The calibrated vapor densities from each method are broken down into low and high frequency parts, the partition being 1.0 Hz, the sampling frequency of the EG&G instrument. The rationale for choosing a cutoff value

NCAR method	Chilled Mirror Instrument (EG&G)	RAF Empirical Curve (Laboratory standard)
FGP method	Chilled Mirror Instrument (EG&G)	Chilled Mirror Instrument (EG&G)
	Low Frequency Signal ("Slow Response")	High Frequency Signal ("Fast Response")

Figure 2.2: Frequency dependent methods for correcting Lyman-alpha data.

of 1.0 Hz is based in part on the sensitivity of the curves to the choice of filter cutoff frequency and is discussed in Section 2.2.6. The major contributor to the calibration slope is indicated for each quadrant. The EG&G is responsible for shaping the low frequency portions of both series. By definition, the EG&G controls the high frequency portion of the FGP corrected vapor density as well. Because the NCAR method leaves the high frequency portion of the data untouched by calibration, the upper right-hand quadrant of the matrix is determined by the original Lyman-alpha signal.

The Lyman-alpha voltages and chilled mirror humidities are processed according to the FGP method previously outlined and a calibration slope and intercept are produced (S_{FGP} and Y_{FGP}, respectively). The NCAR corrected absolute humidity data is regressed against the Lyman-alpha voltage response to give a second pair of calibration coefficients (S_{NCAR} and Y_{NCAR}). These two pairs are determined for several level flight legs and interpreted using the proposed frequency response matrix to characterize the overall similarity between the two calibration methods.

To complete the low-frequency portion of the frequency response matrix, each corrected series is low-pass filtered using the same linear filter as that used in the FGP calibration method. Because the chilled-mirror data will be used as a comparison, this series is interpolated to increase its frequency and then is low pass filtered as well. The resulting filtered, corrected Lyman-alpha time series are then linearly regressed against the filtered chilled-mirror response. The high frequency portion of the matrix is completed in a similar manner. Both of the corrected vapor density series and the raw Lyman-alpha time series are high-pass filtered using the same filter as before. The resulting filtered vapor density series are regressed against the high frequency portion of the Lyman-alpha signal. The regression slopes and standard deviations provide a means by which the methods may be compared.

2.4.5 Discussion

2.4.5.1 Calibration slopes

Twenty-five level flight legs were calibrated using the FGP method. For these same twenty-five legs, the NCAR corrected loose coupled vapor density was regressed against the raw Lyman-alpha voltage. The slopes of the resulting calibration curves were then compared.

	Maximum	Minimum	Mean
Empirical curve	0.283	0.216	0.255
NCAR method	0.250	0.185	0.228
FGP method	0.249	0.127	0.205

Table 2.1: Variation of calibration slopes obtained for each calibration method. Units are in Vm^3/g. "Empirical curve" refers to the RAF curve of Figure 2.1.

We find that there are large differences in the results of the two calibration methods. Within the range of voltages represented in the legs calibrated, the variation in the slopes from the appropriate section of the empirical curve, from the NCAR calibration, and from the FGP calibration method are shown in Table 2.1. Not only are the averages of the slopes different, but there is no consistent trend to note between differences in the individual methods. For example, the FGP method does not consistently produce lower calibration slopes than the NCAR method. Furthermore, there is no apparent height or temperature dependence of the calibrations (Figures 2.3 and 2.4). The overall deviation of the calibration slopes from the expected value may be attributed to a shift in the calibration curve due to temperature. It will be shown that the finer difference, that between the individual slopes resulting from the two calibrations is a result of differences between the NCAR and FGP methods.

2.4.5.2 Frequency response matrix

To determine the source of the difference in slopes, it is useful to divide the results of each method into high frequency and low frequency parts. In this way, a frequency dependent calibration matrix may be developed. Based on the nature of both methods, the low frequency parts of both series should match the slow response vapor density recorded by the chilled mirror instrument. We expect that any differences between the two calibration methods should only be evident in the high frequency portion of the signal.

The similarity of the low frequency portions of ρ_{FGP} and ρ_{NCAR} is shown by a regression analysis where the low pass filtered EG&G data is regressed against the low pass filtered corrected Lyman-alpha data. The high frequency series are treated similarly. Resulting comparisons are listed in Figure 2.5 for both the low frequency and high frequency portions of all sixty-eight legs of corrected data. A1though the absolute difference in the two slow-response regression slopes is slightly more than 10 percent,

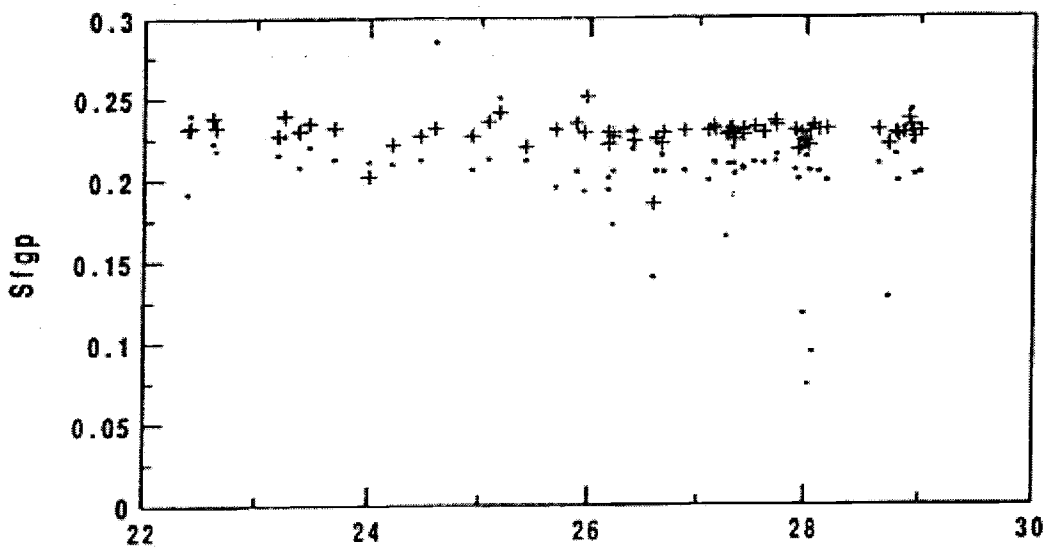

Figure 2.3: Dependence of calibration curves on temperature for all legs. Plusses represent loose couple calibration method and dots represent FGP method.

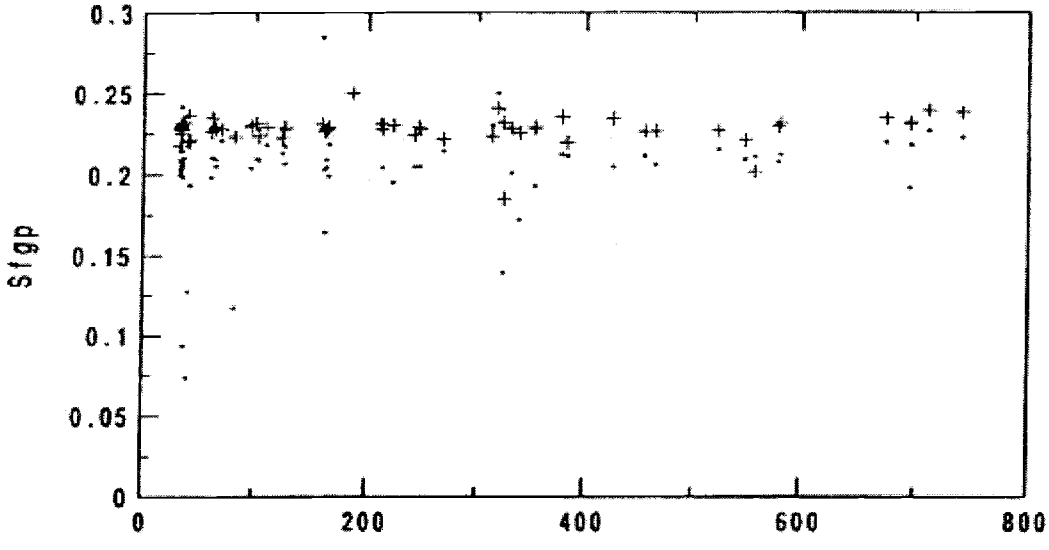

Figure 2.4: Dependence of calibration curves on height for all level legs Plusses represent loose couple calibration method and dots represent FGP method.

the ranges covered by the standard errors in each calculation overlap significantly. Due to this overlap, the low frequency portions of the corrected data are indistinguishable. This may be reinforced by a similar analysis involving the low frequency portions of the raw Lyman-alpha data and the corrected series.

	Slow Response (ρ_{dv})	Fast Response ($V_{L\alpha}$)
ρ_{NCAR}	Slope = 0.891 ± 0.1963	Slope = 4.350 ± 0.0029
ρ_{FGP}	Slope = 1.010 ± 0.2262	Slope = 5.054 ± 0.0019

Figure 2.5: Results of frequency dependent regression analysis for all sixty-eight flight legs.

A similar method of analysis verifies that the two high frequency portions of the corrected data are not equivalent. Each slope has a standard error of order 0.001. However, they differ from each other by about 15 percent, so the ranges covered by these two values do not overlap. It is because of this that the high frequency portions of the data are distinguishable and may therefore be considered unequal. Fluxes computed from the calibrated Lyman-alpha data depend linearly on the slope of the calibration curve:

$$V_{L\alpha} = Y + S\rho_v$$

as follows:

$$E = \overline{w'\rho_v'} = S\overline{w'V_{L\alpha}'}$$

This means that, for the data considered here, the computed fast response vapor *fluxes from the NCAR method will be lower than the FGP fluxes by as much as 10%.*

To complete the matrix, it is noted that, by the nature of the FGP method, the high and low frequency parts of ρ_{FGP} are determined by the chilled mirror instrument, and are therefore equal. Thus, the low frequency ρ_{NCAR} and the high frequency ρ_{NCAR} must not have the same voltage/water vapor density response curve. Not only does this reinforce the statement that the NCAR method matches baseline vapor densities without affecting the high frequency output of the Lyman-alpha (Schanot, (1987)), it shows that the difference in the overall calibration slopes is due to the difference in treatment of the high frequency data.

2.4.6 Additional checks on the FGP method

Because the result of the FGP method may depend on factors introduced in the processing, some additional checks were made. The two factors investigated were the dependence of calibration slope on filter cutoff frequency and the effect of an increase in correlation sampling length on the calculated lag. A short discussion of the methods and results of these checks follows.

2.4.6.1 Filter Cutoff

The dependence of the calibration curve on filter cutoff was checked by varying the filter cutoff frequency and comparing the resulting coefficients for several flight legs. It was shown that for frequencies below the Nyquist frequency of the slow response instrument, 0.5 Hz, the calibration slope changes drastically with cutoff frequency. For cutoff frequencies greater than 0.5 Hz, the calibration slope dependence rapidly drops off.

The objective of the filter is to partition the low frequency and high frequency portions of the Lyman-alpha signal. At frequencies lower than 0.5 Hz, the slow response instrument is all that is determining the calibration of the data. Because the filter is not perfect, the filtered data with a 0.5 Hz cutoff frequency contains some slow response information in the high frequency band. A cutoff frequency of 1.0 Hz was

used across the board for the calibrations to "clean up" the low frequency signal without disguising the hysteresis loops present in the scatter plot of chilled mirror vapor density vs. Lyman-alpha voltage prior to shifting the data (Friehe et al. (1986)). Since the correlation between the Lyman-alpha and chilled mirror data is expected to occur below 0.5 Hz, the introduction of higher frequency data through the less-than-ideal filter does not adversely affect the calibration.

2.4.6.2 Lag Calculation

To compute the lag between the chilled-mirror instrument and the Lyman-alpha instrument, the first five seconds of data (100 samples) were correlated to determine the lag. In high humidity applications, the expected response time of the EG&G sensor is approximately two seconds (Schanot (1987) and Spyers-Duran and Schanot (1987)). Because of the consistently high humidities, any increase in the correlation value beyond a time of five seconds is most likely due to sampling error. In all cases, the calculated lag was, as expected, less than two seconds.

2.4.7 Comparison of Lyman-alpha and UV hygrometers

The UV hygrometer is an experimental instrument that was being tested for airborne measurement of vapor flux on the Electra during TOGA COARE. It was in place next to the Lyman-alpha and operable during flights RF20 and RF21. Between those flights, a total of 14 legs were found where both instruments simultaneously appeared to be working. There were five additional legs between the two flights, but there were flat portions in the instrument response for either the UV instrument or the Lyman-alpha indicating that one instrument was inoperable. The voltages obtained from the instruments were calibrated and archived as mixing ratios at NCAR.

	Maximum	Minimum	Mean	Error
Chilled-mirror	20.100	16.560	18.420	0.596
Lyman-alpha	19.510	16.600	18.340	0.564
UV hygrometer	19.820	16.640	18.460	0.606

Figure 2.6: Mean and range of block-averaged values of mixing ratio measured by various instruments. Units are in kg/m^3.

A very basic analysis of the curves was done to determine relative magnitudes of the measurements. Block averages were used to determine relative positions of the curves because it was noted that positions were not consistent throughout a given flight leg. Blocks of 150-second duration (one-half of a mesoscale cycle) were chosen and averages were calculated for each instrument (Figure 2.6). The resulting averages were subtracted to determine the mean actual differences listed in Figure 2.7. This figure also shows that there is no apparent bias between the UV hygrometer and either of the other instruments. There is, however, a tendency for the Lyman-alpha mixing ratio to be higher than that measured by the chilled-mirror instrument. This bias is not a concern, though, because the average difference between the calculated mixing ratios is less than one percent.

Statement	Percentage true	Mean actual difference	
La > UV	44.4%	0.117 kg/m^3	0.646
La > CM	35.2%	0.080 kg/m^3	0.429
UV > CM	54.6%	0.0.37 kg/m^3	0.211

Figure 2.7: A measure of the relative position of the Lyman-alpha, UV hygrometer, and Chilled mirror response curves.

2.4.8 Conclusion

NCAR's method of loosely coupling the EG&G vapor density measurement to the response of the Lyman-alpha hygrometer is determined to be significantly different from the method of linear calibration proposed by Friehe et al. (1986). Though the two methods reference the fast response data to the trusted slow response instrument and, thus, give essentially the same water vapor densities at low frequencies, they have very different effects on the resulting high frequency signals.

We have chosen the NCAR method for our analysis of the turbulent water vapor fluxes. First, the NCAR method provides an objective criterion for decoupling the high and low frequency data. The loose-couple method is set by design to "decouple" in cases where there is a dramatic change in ambient moisture (Schanot personal communication (1994)). When the slow response vapor density is changing rapidly, data from the Lyman-alpha is questionable (Schanot (1987)) and may yield inaccurate turbulent fluxes. The FGP method does not include an inherent comparison of the trends in the slow and fast-response instruments. That is, it is not capable of independently checking for discontinuities in either instrument's signal.

Second, the NCAR method can be applied to a wider range of conditions. The FGP method is limited to use only for level flight legs of reasonable length.

Third, the resulting calibration is subject to the sensitivity of the calibration curve to the choice of filter cutoff frequency and to the correct calculation of the slow response instrument's time lag. Slow response calibration coefficients are applied to the fast response data and there is no system of checks on the FGP method to ensure that the integrity of the raw Lyman-alpha data is maintained. For the TOGA COARE data investigated here, with high humidities and temperatures, the result is, on the average, larger turbulent vapor densities than those calculated by NCAR's method.

This is not to say that the NCAR method is without its shortcomings. Although the coupling history of the corrected series serves as a check for the validity of the data (Schanot, (1987)) and the fast response portion of the data series remains untouched by the calibration, the NCAR method is applied in a batch mode, and therefore cannot compensate completely for the response lag of the slow response instrument. The resulting vapor density fluxes will tend to be lower, but since the slow response portions of both sets of corrected data match and the presence of the slow response lag is the NCAR method's only major shortcoming, we believe that the NCAR method is the more reliable of the two methods for purposes of turbulent water vapor flux estimates.

3. Surface Evaporation Estimates by Method of Eddy Correlation

3.1 Eddy correlation method

Eddy correlation flux is a relatively simple flux calculation method that relates time series or perturbations to one another. It is a desirable method for flux calculation because it directly relates fast response data to transfer of sensible heat, without need for assumptions of similarity theory. The difficulty posed by direct flux measurement is the difficulty of using response instruments and obtaining an adequate sample of the flux-carrying eddies.

Once the time series has been inspected for erroneous data, the time series may be demeaned or detrended to yield a series of perturbations (denoted by primes):

$$\phi'(t) = \phi(t) - \bar{\phi}$$

where actual measured values are denoted by f(t) and the overbar indicates a local mean value:

$$\bar{\phi} = \frac{1}{\lambda}\sum_{i=1}^{\lambda}\phi_i \tag{3.1}$$

Once the individual perturbation time series are computed from a set of data, the kinematic flux may be simply obtained as an ensemble average of their products:

$$F = \langle w'\phi' \rangle \tag{3.2}$$

where the angle brackets indicate the average over distance L (see section 3.1 for a discussion):

$$\langle F \rangle = \frac{1}{L}\sum_{i=1}^{L}F_i \tag{3.3}$$

Kinematic fluxes relate to sensible and latent heat as follows:

$$H = \rho C_p \left\langle \overline{w'T'} \right\rangle$$
$$E = \rho L_v \left\langle \overline{w'q'} \right\rangle$$

Where ρ is the density of air, L_v is the latent heat of vaporization for water, and C_p is the specific heat for moist air. Variation in C_p with changes in humidity is neglected here. This could result in up to 10% error in H (Stull). According to Sun et al (1995), the sensible heat flux introduced by variation in C_p with changes in humidity over the ocean is actually smaller than that, generally less than a few percent of the total sensible heat flux. They go on to say that it becomes large relative to total sensible heat flux only in "cases of maximum solar forcing of a saturated land surface". Perturbations of vertical velocity, temperature, and water vapor mixing ratio, are denoted by w', T' and q' respectively.

When averaging, it is not necessary for λ to equal L, but λ must be greater than or equal to L (in other words, L must be the size of a subset of λ). We will show that, to include 90% of the turbulent flux, L must increase with height from 1 km at the surface to 3 km near the top of the boundary layer. Chapter 5 uses this result to explore the equivalence of bulk flux estimates to eddy flux estimates at various altitudes. The "record length" λ is chosen to be 20 km to obtain an adequate sample of flux-carrying eddies.

3.2 Averaging length

Scale dependence of fluxes has been a focus on attention in turbulence research in recent years (Howell et al. (1997), Sun et al. (1996), Lenschow et al. (1994), Williams et al. (1996)). In the estimation of leg averaged flux, there may be two different length scales: the local averaging scale L, and the record length λ. Mesoscale circulations are ubiquitous in the atmosphere and TOGA COARE, thus aircraft data is likely to include a significant contribution due to mesoscale circulations. In order to

isolate the turbulent flux (or eliminate 'mesoscale bias'), it is desirable to choose a local averaging scale that adequately samples the flux carrying eddies. These smaller scale fluxes may then be averaged over λ to determine a leg averaged turbulent flux. Because circulations occur on a continuum of scales, the choice of L is somewhat arbitrary with its arbitrariness governed by the amount of the turbulent flux desired weighed against the error introduced by mesoscale bias. Local averaging scale is not simply an arbitrary function of height, however. Rational selection criteria are discussed in section 3.2.

The eddy correlation fluxes for the C130 are the ordered products of deviations from means (over distance L) of two time (or space) series averaged over a distance λ. In homogeneous conditions, the choice of length scale over which the local means are calculated is of little consequence other than to increase statistical certainty as long as it is sufficient to include turbulent motions. In inhomogeneous cases, however, there becomes a concern not only about including turbulent transport in the flux calculations, but also about excluding any contribution due to mesoscale circulations. Several scientists (Howell et al. (1997), Howell (1995), Lenschow et al. (1994), and Friehe et al. (1991)) have addressed this problem.

In this study, the eddy correlation values of sensible and latent heat flux were calculated in a conventional manner. The idea behind eddy correlation is that deviations from series mean values for two time series are first used to compute a series of ordered products, say $w'\phi'$, the 'instantaneous flux'. This instantaneous value is then averaged over some distance (or time), λ, to obtain an estimate for the eddy correlation flux. The averaging length λ represents the scale of motions included in the estimate.

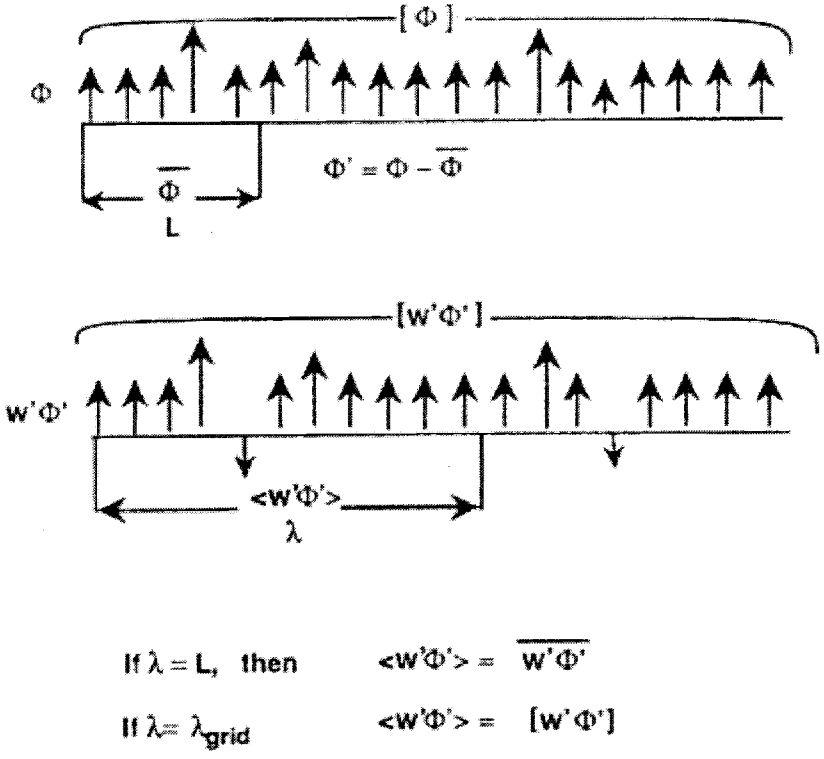

Figure 3.1: Schematic of averaging lengths L and λ for variable ϕ (from Sun et. al (1996)). Each vertical arrow represents a discrete value of ϕ and w'ϕ', respectively.

The method of calculating the mean values both of the original time series and of the flux has received some attention in recent years. Sun et al. (1996) contend that the vertical fluxes of heat and moisture depend on the choice of "cut-off length scale [L] and flux averaging length scale [λ] . . . and method of calculating the flux. They suggest that an intelligent choice of length scales will include the majority of the turbulent flux while eliminating errors induced by inclusion of mesoscale motions in the calculation.

There are a couple of ways in which L may be determined either 1) by a spectral analysis of the fluxes (Friehe et al. (1991), Lenschow et al. (1994), Williams et al. (1996)) or 2) by evaluation of the flux covariance as a function of L directly (Howell, (1995)). Power spectra of fluxes in the atmospheric boundary layer can be hard to interpret without smoothing or averaging (pers. comm., J. Howell, (1996)) so the latter method is chosen for this study.

The method that we will use to select the length scales is described in detail by Sun et al. (1996). For low level flights, a cut-off length scale, L (i.e., that which is used in calculating fluctuations) of 1 km is appropriate and it will be shown that this cutoff length scale increases with increasing altitude. In homogeneous conditions, a flux averaging length scale, λ, that is longer than L serves to decrease the statistical error of a given flux estimate. However, in heterogeneous conditions, increasing λ beyond the size of L increases the chance that the local characteristic of the flux changes within that length and thus increases the variance of the final measurement. It is for this reason that both length scales, L and λ, will be equal unless otherwise noted (e.g. in chapter 3).

Based on natural breaks in the distribution of altitude, 163 of the 168 flight legs evaluated in Chapter 1 were divided into the following height categories: 25-35 m, 35-40 m, 40-50 m, 60-70 m, 90-110 m, 150-250 m, 300-400 m, and 450-800 m. Legs above 800 m average height were excluded. This distribution of sample spacing is desirable because of the logarithmic nature of the profile functions and is possible

because of the concentration of flights in the near-surface layer during TOGA COARE. The change in flux between two length scales is calculated as follows:

$$Change = \frac{\Delta Flux}{\Delta \log(L)} \tag{3.1}$$

and is a fairly useful tool in determining the physical significance of the results that follow. In representing the rate of change of the flux, ΔFlux is Flux(L) - Flux(L-1) and Δlog(L) is simply log(L) - log(L-1), an analogy to Fourier spectral analysis methods.

Composites of leg averaged fluxes (Figures 3.2(a), 3.3(a), 3.4(a), and 3.5(a), cumulative latent heat flux (E) and sensible heat flux (H) were constructed for all legs in each category longer than 50 km in length. The specific method used is outlined in Howell (1995) and has also been used in Sun et al. (1996).

Consistent with Sun et al. (1996), all altitudes within the mixed layer (below 300 m) reveal the same characteristic shape in cumulative flux. For latent heat at these altitudes, there is a drastic increase in flux up to scales of L~1 km, after which the flux levels off. This increasing trend is visible in the rate of change frequency spectrum (Figures 3.2b, 3.3b, 3.4b, and 3.5b) as a sustained minimum. At heights above 600 m, this same early increase is visible in latent heat flux, though not as drastic. In the mixed layer, sensible heat flux increases over scales up to L~1 km and levels off in a manner similar to the latent heat flux at the same levels. At altitudes above 600 m, however, the sensible heat flux is always negative indicating downward transport of heat.

The rate of change of cumulative flux is shown in Figures 3.2(b) and 3.3(b) for latent heat flux and in 3.4(b) and 3.5(b) for sensible heat flux. For all flights in the surface layer, the leg-averaged flux increases rapidly for lengths less than ~O(0.1 km) and by the time L~O(1km), the change in leg-averaged flux becomes small. At scales on the order of 10 km and larger, motions of scale smaller than the record length, but

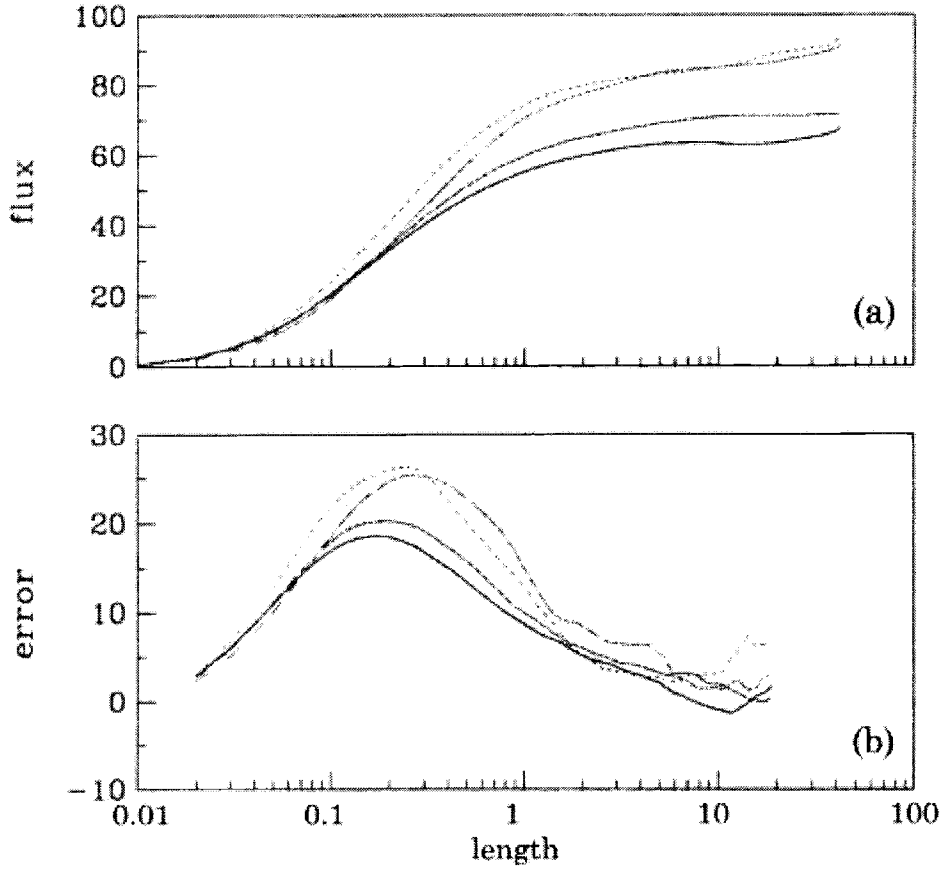

Figure 3.2: Composite latent heat flux (a) and rate of change of cumulative flux (b) for flights below 90 m. The solid line represents flights between 25 and 30 m, the dashed line represents those between 35 and 40 m, the light dotted line represents 40 to 50 m, and the dotted line represents 60 to 70 m.

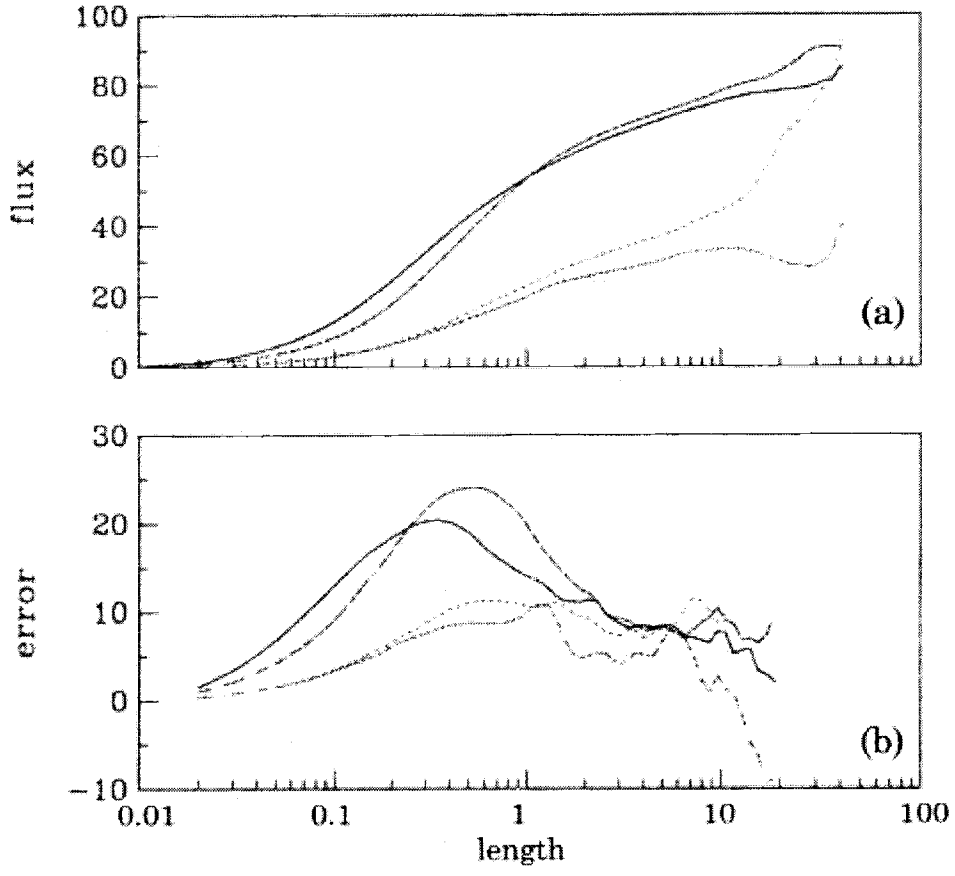

Figure 3.3: Composite latent heat flux (a) and rate of change of cumulative flux (b) for flights above 90 m. The solid line represents flights between 90 and 110 m, the dashed line represents those between 150 and 250 m, the light dotted line represents 300 to 400 m, and the dotted line represents 450 to 800 m.

larger than turbulent scales are included and increase the variability of the cumulative flux. We see variability in the cumulative flux rate of change at scales above 5 km as well, due to the limited length of the flight legs.

Latent heat flux in the surface layer behaves in a manner consistent with Sun et al (1996). At least 90% of the turbulent flux for flights below 40 m is contained at length scales (L) less than 1 km. Although the peak in the difference curve shifts toward larger L as altitude increases, L=1km is still sufficient to describe approximately 90% of the flux even at altitudes up to 70 m. Between 90 and 250 m, however, the curves have shifted too far to the right and it becomes judicious to increase the local averaging length scale to L=2km. Sampling errors introduced by the relative size of L and the leg make the curves difficult to interpret above 300 m. The variability around L=10km and larger is, as mentioned previously, due to limited sampling of large-scale motion. That is, simply too few motions of this size are sampled to result in a reliable estimate of the flux. At approximately 3 km, though the cumulative flux is still increasing, the curve has not yet become erratic. This cutoff, though not necessarily indicative of 90% of the flux, is likely to be the point at which the gain in turbulent flux measurement is offset by uncertainty introduced by the inclusion of larger scale motions.

Sensible heat flux does not seem to follow such a consistent convention. Again, at altitudes below 90 m, the curves shift to the right as altitude increases and they have the same characteristic shape as the latent heat flux at small L. Like the latent heat curves, L=1km is sufficient at low altitudes to include 90% of the turbulent flux (again, consistent with Sun et al., 1996). At altitudes above 100 m, the majority of the change in cumulative flux still occurs at scales smaller than 1 km. This interpretation of flux variability with length becomes questionable in the 90 to 110 m region.

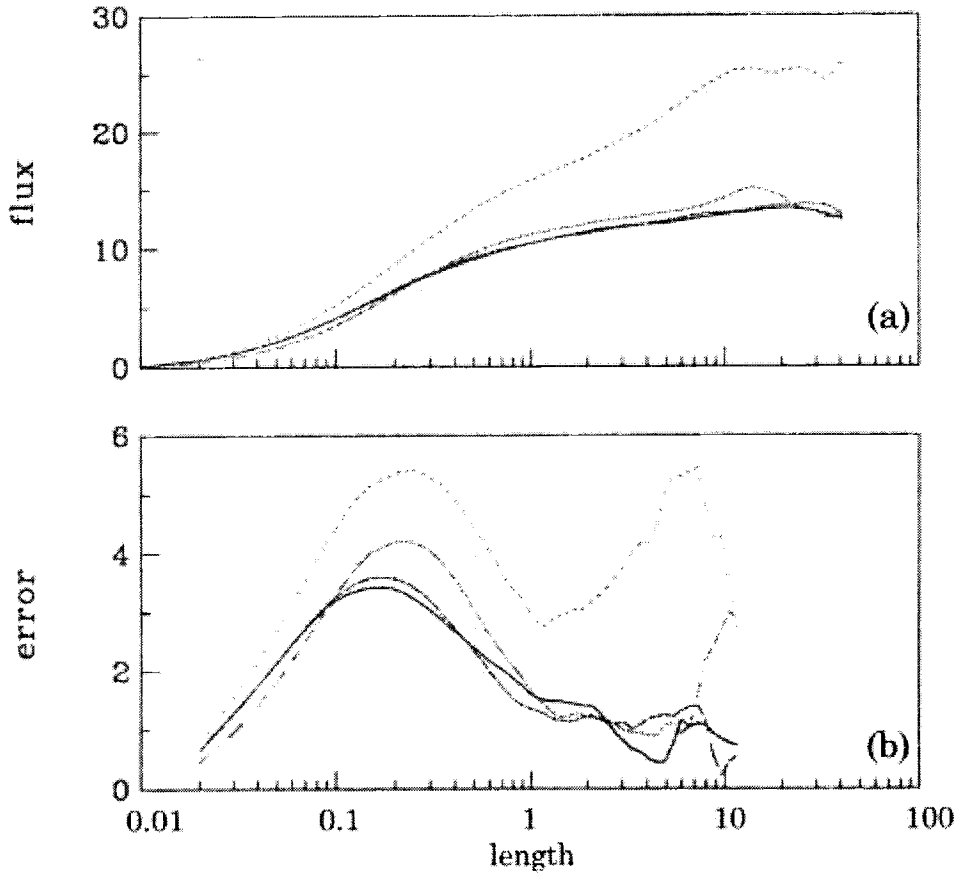

Figure 3.4: Composite sensible heat flux (a) and rate of change of cumulative flux (b) for flights below 90 m. The solid line represents flights between 25 and 30 m, the dashed line represents those between 35 and 40 m, the light dotted line represents 40 to 50 m, and the dotted line represents 60 to 70 m.

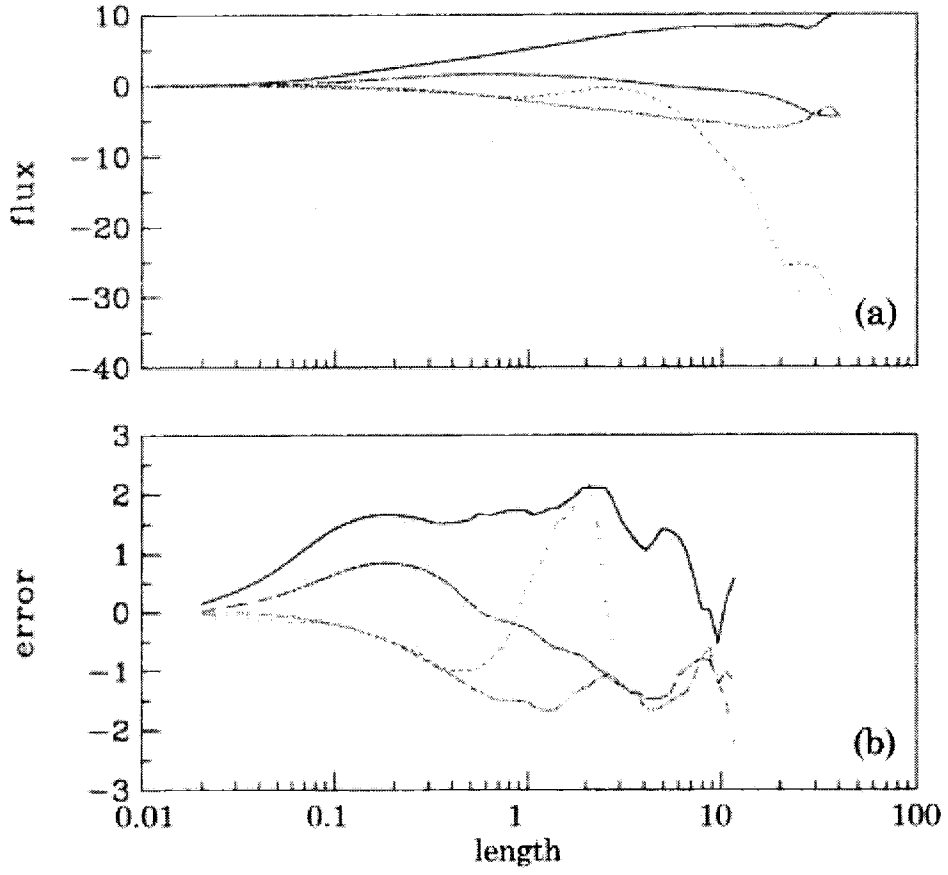

Figure 3.5: Composite sensible heat flux (a) and rate of change of cumulative flux (b) for flights above 90 m. The solid line represents flights between 90 and 110 m, the dashed line represents those between 150 and 250 m, the light dotted line represents 300 to 400 m, and the dotted line represents 450 to 800 m.

Between 90 and 110 m, the cumulative flux curve is relatively straight between L=0.1km and L=10 km on a log scale (slope ~ 7/3). Only at L=10 km does it level off as seen with the other curves. This continuous increase can be attributed to the sampling of a continuous range of large-scale motions. Most of these flights took place on light winds where buoyancy (and therefore large eddies) dominates vertical transport of heat. It seems logical, however, to conclude that L=1km would, over a more varied sample of flights, include the majority of the flux since L=1km is clearly sufficient from the figure to resolve motions in the flights between 150 and 250 m. This is a warning that in cases of light winds and strong surface heterogeneity problems may arise in eddy correlation measurements of the flux. These problems may be enhanced at higher altitudes because eddies can cover a larger range of magnitudes than can eddies at the surface.

Above 300 m, the sensible heat flux is negative. The conventional profiles (Stull, 1988) predict a change in sign of sensible heat flux at $z/z_i \approx 0.7$, or 400 m in the tropics. Also, as the averaging length scale increases, one would expect the cumulative flux to become more negative because the transporting eddies are removing heat from the atmospheric boundary layer. Thus, the minima in the difference curves reveal the fastest change in the cumulative flux. Applying this reasoning, a 2 km local averaging scale still appears sufficient for flights between 300 and 400 m, but above 400 m we see the same problem as we saw with the latent heat flux. The difference begins to vacillate about some nonzero value without any real approach to zero. Thus the choice of length scale above 400 m becomes somewhat subjective. Again, L=3 km is chosen because, based on the rate of change curve, it appears sufficient to include a large portion of the turbulent flux while excluding the majority of mesoscale motions.

4. The Bulk Aerodynamic method and COARE Algorithm

4.1 The bulk aerodynamic method

Similarity theory is a method by which meteorological variables can be grouped and nondimensionalized to create "universal" relationships. These relationships (flux as a function of altitude, for example) can them be used to estimate surface fluxes. For example, the profiles of potential temperature, specific humidity, and wind in the surface layer as a function of altitude exhibit a consistent characteristic shape over a variety of conditions, regardless of the actual height of the surface layer. It is possible, then, to introduce a scaling parameter which nondimensionalizes the height. Assuming these curves and their governing parameters are universal, this empirical result may be applied to other situations. It is empirical curves determined in this way (specifically nondimensional wind shear and nondimensional lapse rates of temperature and specific humidity) that are used in the COARE algorithm in determining the bulk transfer coefficients. The reader is referred to Panofsky and Dutton (1984) and Stull (1988) for an in-depth review of similarity theory. An overview of one method, Monin-Obhukov similarity as it applies to TOGA COARE is presented here.

Monin-Obhukov similarity theory introduces scaling parameters for friction velocity (u_*, see Stull (1988)) and length (L) where the length is a function of friction velocity and heat flux. It states that, when the covariances and profiles of atmospheric parameters are normalized by these scaling variables, they become universal functions of z/L where L is the Obhukov length:

$$L = \frac{-\overline{\theta_v} u_*^3}{kg(\overline{w'\theta_v'})_s}$$

and k is the von Karman constant, g is the acceleration due to gravity, θ_v is the virtual potential temperature, and

$$\frac{g}{\overline{\theta}_v}\left(\overline{w'\theta_v'}\right)_s$$

is the buoyancy flux.

One of the constraints on the validity of Monin-Obhukov similarity theory (and therefore on the bulk aerodynamic method for turbulent flux estimation) is that the flux in the surface layer varies by less than 10% of its magnitude over the surface layer depth, implying a layer of approximately constant flux (e.g., Stull (1988)). This results in two limitations on its use. First, similarity theory is best suited for use in conditions of moderate winds and there is uncertainty in the bulk coefficients for neutral conditions where wind speeds are less than 0.5 m/s. A correction must be made for buoyancy effects on turbulent transport in light winds. Second, the method of similarity only applies to the surface layer where length scales are less than the Monin-Obhukov length scale (e.g., flights below ~100m). In this study, we will evaluate the validity of this assumption during TOGA COARE. The remainder of this section outlines the bulk aerodynamic method, followed by specific features in the COARE algorithm used to compute data values used in this paper. These calculations will then be compared to eddy correlation fluxes in the remaining chapters of the paper.

The bulk aerodynamic method is a parameterization scheme that relates surface flux to wind speed and the bulk vertical gradients of specific variables by means of similarity theory. The theory predicts that the fluxes are proportional to the mean wind speed and the relative value of a specific state variable:

$$\left(w'T'\right)_s \propto \overline{U}\left(\overline{T} - T_g\right)$$
$$\left(w'q'\right)_s \propto \overline{U}\left(\overline{q} - q_g\right)$$

where w', q', and T are the turbulent fluctuations of vertical wind, water vapor mixing ratio, and temperature, respectively, and the overbar denotes an ensemble average (in

this case, a temporal average is used). T_s and q_s are the sea surface temperature and surface mixing ratio (corrected in the COARE algorithm for typical ocean salinity). The horizontal wind speed, temperature, and mixing ratio at some reference height, z, are indicated by u, T, and q. Bulk transfer coefficients are introduced to change the above relationships into equivalencies. The transfer coefficients, in unstable situations, are determined using similarity relationships (Fairall et al (1996)).

Monin-Obhukov similarity is the basis for estimating fluxes in the COARE algorithm and, as was alluded to before, it breaks down in cases where the friction velocity approaches zero, but the buoyancy flux does not. Simply stated, as buoyancy begins to dominate heat transfer in the surface layer and we approach the free-convective limit, traditional Monin-Obhukov similarity approaches a singularity and meaningful transfer coefficients can not be obtained.

There are two possible ways to deal with this problem outlined in the literature. First, one could empirically measure the transfer coefficients (see Liu et al., 1989 for a discussion). The alternative approach is to use a scalar wind speed, rather than vector magnitude, in computing transfer coefficients and stability parameters. This so-called gustiness correction is applied in the COARE algorithm. A brief overview is provided in section 4.4, but the reader is referred to Fairall et al. (1996) for a more complete discussion of the COARE algorithm.

4.2 Notation

Throughout the following chapters, there will be references to three distinct methods of calculating the flux using the bulk method: total flux, scalar flux, and vector flux. There are two separate averaging lengths as well: L and λ. L indicates the leg-averaged flux and is denoted in the bulk formulas with angle brackets, <>:

$$\langle (\cdot) \rangle = \frac{1}{L} \sum_{i=1}^{L} (\cdot) i \tag{5.3}$$

Local ensemble averages, λ, are denoted by overbars. The bulk formulae are as follows (after Esbensen & McPhaden, (1996)):

Total Flux:

$$\begin{aligned} \langle E \rangle &= \overline{\rho}\left\langle C_E \overline{U}\left(\overline{q_{sfc}} - \overline{q}\right)\right\rangle \\ \langle H \rangle &= \overline{\rho}\left\langle C_H \overline{U}\left(\overline{T_{sfc}} - \overline{T}\right)\right\rangle \end{aligned} \tag{5.4}$$

Scalar Flux:

$$\begin{aligned} E_s &= \overline{\rho} C_E \langle \overline{U} \rangle \left(\langle \overline{q_{sfc}} \rangle - \langle \overline{q} \rangle \right) \\ H_s &= \overline{\rho} C_H \langle \overline{U} \rangle \left(\langle \overline{T_{sfc}} \rangle - \langle \overline{T} \rangle \right) \end{aligned} \tag{5.5}$$

Vector Flux:

$$\begin{aligned} E_v &= \overline{\rho} C_E V \left(\langle \overline{q_{sfc}} \rangle - \langle \overline{q} \rangle \right) \\ H_v &= \overline{\rho} C_H V \left(\langle \overline{T_{sfc}} \rangle - \langle \overline{T} \rangle \right) \end{aligned} \tag{5.6}$$

where $\langle U \rangle = \left\langle (\overline{u}^2 + \overline{v}^2)^{1/2} \right\rangle$ and $V = (\langle \overline{u} \rangle^2 + \langle \overline{v} \rangle^2)^{1/2}$ are the scalar and vector averaged windspeeds. Mesoscale enhancement of the latent and sensible flux is defined to be $\Delta E \equiv \langle E \rangle - Ev$ and $\Delta H \equiv \langle H \rangle - Hv$, respectively. Physically, mesoscale enhancement refers to the discrepancy arising between the vector averaged and total flux estimates due to mesoscale disturbances. In the absence of mesoscale motion, one would expect ΔE and ΔH to be zero. Actual results for the TOGA COARE region are presented in chapters 5 and 6.

All bulk fluxes in this study are calculated using the COARE algorithm, regardless of the method of obtaining horizontal windspeed. For simplicity, it is assumed that ρ, C_p, and L_V are all constant and equal 1 kg/m^3, 1005 J/kg°K, and 2500

J/g respectively. Fluxes are calculated using the algorithm-produced scaling variables u*, T*, and q* and the following relationships:

$$E = -\rho_a L_v u_* q_*$$
$$H = -\rho_a c_p u_* T_*$$

There is no moisture correction term as it is negligible in this application (Sun et al. (1995)). The cool-skin, warm layer corrections in the algorithm are turned off as well since the sea surface temperature was measured by a downward looking radiometer (Fairall et al., (1996)).

In contrast to Esbensen and McPhaden who use hourly averages for the local average, λ, and daily averages for the large scale average, L, this study uses 1 km and 50 km for the respective averaging lengths on low-level flight (compared to L=λ=10km in Vickers and Esbensen (1998)). The local averaging length scale needs to be sufficiently long to adequately sample turbulent eddies without introducing errors due to mesoscale motions. It was shown in Section 3.1 and by Sun et al (1995) show that for low level flight legs over the COARE region 1 km is sufficient to resolve the turbulent motions. As defined in Section 3.1, 2 km and 3 km are used where appropriate as the altitude increases. The continuous nature of the scales of motion in the real world makes the choice of 1 km rather arbitrary. Williams et al (1996) uses 2 km with the reasoning that the spectral effects of small-scale processes cease at scales above 2 km, but they also mention that this scale can increase at higher altitudes. Sun et al (1996) uses a similar reasoning in estimating that 90 percent of the turbulent flux resides at scales below 1 km for low-level flights. Clearly, there is some subjectivity in the choice of local averaging length scale. The specifics and implications of this question were addressed in Section 3.1.

Bulk fluxes were computed using the COARE algorithm (Fairall et al. (1996); section 4.2) with 1-km averaged data as inputs. The resulting scaling variables, u_*, T_*,

and $q*$ were then multiplied for each segment and averaged over 20 km to obtain 20 km averaged bulk estimates of the turbulent flux:

$$\langle w'q' \rangle = -u_* q_* \qquad \langle w'T' \rangle = -u_* T_* \qquad (4.1)\ \&\ (4.2)$$

In equations 4.1 and 4.2, the angle brackets indicate the leg averaged flux and $u*$, $q*$ and $T*$ are the similarity scaling parameters for velocity, mixing ratio, and temperature, respectively. For consistency between the bulk and eddy fluxes, physically representative values for the fluxes (values in W/m^2) were obtained by multiplying the evaporation (in mg/s·kg) by 2500 kJ/m^3 and the sensible heat (in Km/s) by 1005 J/m^3K corresponding to nominal values of the latent heat of evaporation (L_v) and the specific heat of air at constant pressure (C_p), respectively. That is:

$$E_{bulk} = -\rho L_v u_* q_* \sim -2500 u_* q_* \qquad H_{bulk} = -\rho C_p u_* T_* \sim -1005 u_* T_* \qquad (4.3)\ \&\ (4.4)$$

4.3 The COARE algorithm

Version 2.0 of the COARE algorithm is based on Monin-Obhukov similarity theory, specifically based on the model developed by Liu et al. (1979), but with several modifications. The algorithm combines a correction for the singularity present in traditional Monin-Obhukov similarity due to buoyancy effects (after Liu et al. (1979)) using a gustiness velocity (after Godfrey and Beljaars (1991)) to account for the effect of light winds (less than 0.5 m/s) prevalent in the western Pacific warm pool (Fairall et al. (1996)). Additional modifications were made by Friehe et al (1996) to address (after Smith (1988)) and corrections to the boundary conditions at the ocean-atmosphere interface (the contributions of mean vertical wind to heat flux and of precipitation to the sensible heat flux). As a result, the Monin-Obhukov profile functions for strong

convection were improved, as was the ocean top-layer mixing model. In addition, Fairall et al. (1996) have done a great deal of work to define various physical parameters well (e.g., the von Karman constant and latent heat of vaporization of water). Finally, in the version of the algorithm used in this paper, adjustments have been made to the transfer coefficients to more closely match selected COARE ship data eddy correlation fluxes. An overiew of the corrections pertinent to this study is presented here; for more specific information or details on the remaining features, the reader is referred to Fairall et al (1996) and the other cited references.

4.4 Corrections relevant to this study

4.4.1 Roughness length and gustiness parameter

Corrections in the COARE algorithm that are relevant to this study include inclusion of buoyancy effects (the gustiness correction) and the proper lower boundary condition for the total mass flux (the Webb correction, after Webb et al. (1980)). Cool skin and warm layer corrections to sea-surface temperature were not used, since SST was measured using a downward looking infrared radiometer (Fairall et al. (1996)) and this correction is relevant to temperatures measured with a bulk thermometer.

Due to the empirical nature of the transfer coefficients, there is bound to be some debate over the validity of the similarity relationships. In addition, the applicability of the relationships becomes questionable near or above the top of the surface boundary layer. For example, the bulk method has problems in strongly buoyant conditions and in cases of small surface heat flux. Several scientists have noted that the neutral drag coefficient (and thus heat transfer coefficient) increases in weak winds (Smith (1988), Vickers and Mahrt (1997), and Grachev et al. (1998) to name a few). Specifically, the transfer coefficients are a function of windspeed, boundary layer stability, and wave state and they approach a singularity at wind speeds below 0.5 m/s. As was discussed earlier, buoyancy effects dominate mixing in light winds and the traditional method of similarity becomes invalid. Fairall et al. (1996) use

a combined roughness length (after Smith (1988)) that merges the conclusions that (1) as wind speed decreases below 2 m/s the relationship between the surface roughness and the friction velocity approach a constant velocity (smooth flow) and (2) in rough flows, the surface roughness may be described by the Charnock (1955) formulation. Roughness length in the COARE algorithm is parameterized as:

$$z_0 = \frac{\alpha u_*^2}{g} + 0.11\frac{\nu}{u_*}$$

Where α is the Charnock constant and the neutral drag coefficient is a function of z/z_0. The first ratio on the right hand side of the equation is the rough flow contribution and the second is the smooth flow contribution.

In traditional Monin-Obhukov similarity theory, the determination of the neutral drag coefficient becomes problematic in strongly convective situations. As mentioned earlier, the issue is with the performance of Monin-Obhukov similarity as we approach the free-convective limit; specifically, traditional Monin-Obhukov similarity suggests a fixed direction for the mean wind vector, so, in strongly convective cases where the mean wind nears zero, the theory approaches a singularity (Grachev et al (1988). The COARE algorithm addresses this shortcoming with a gustiness correction after Godfrey and Beljaars (1991). Basically, this corrects for the difference between the average wind speed and the magnitude of the wind vector (a problem seen when convection is buoyancy driven and wind velocity is variable but has no mean velocity). The gustiness correction is used in version 2.0 of the COARE algorithm (Fairall et al (1996)) as a correction in calculating the transfer coefficients and stability parameters, and, ultimately, the bulk flux. Although only 3 of the 68 flight legs have wind speeds less than 0.5 m/s, there are several with speeds below 4 m/s. The results in these "weak wind" cases are compared to eddy correlation fluxes as well as to "strong wind" cases (wind speed greater than 4 m/s) in the chapters that follow.

4.4.2 Webb correction

In cases where heat flux is positive (upward), warmer parcels of air are ascending as cooler ones fall. Although there is no mass transfer of dry air in this situation, there is a small mean upward transport of water vapor, which contributes to the mass flux (Webb et al. (1981)). The so-called "Webb correction" is needed when the concentration of water vapor is expressed as a mass density and becomes important when this mean vertical mass transport contributes significantly to the total vertical heat flux. During the COARE timeframe, this correction averaged 4 W/m^2 (Fairall et al (1996)) and is associated with the small mean upward motion that is present in buoyancy driven convection.

Bulk fluxes used in this study were computed using the COARE bulk flux algorithm, version 2.0 (Fairall et al (1996)). As mentioned, this version of code includes options for a cool skin/warm layer correction and Webb correction, but they were not used. The cool skin/warm layer correction is not needed since the aircraft measures the sea surface skin temperature. The Webb correction is not used for either the bulk or eddy correlation flux estimates. The gustiness correction, however, was used for the bulk flux estimates in this study.

5. Comparison of Eddy Correlation Fluxes and COARE Bulk Fluxes

5.1 Simple error

Inthis chapter, we examine how the fluxes computed with the COARE bulk algorithm compare to those calculated by eddy correlation as a function of height in the boundary layer. Simply stated, the bulk method yields consistently higher flux estimates than does the eddy correlation method (Figure 5.1). A simple hypothesis test that the values are equal on average reveals, however, that they are statistically indistinguishable (with 99% confidence) when the estimates are averaged over all possible legs and altitudes. The statistics change slightly when separated into various altitude categories. In that case, the means are indistinguishable with altitude for all latent heat estimates, but only for those sensible heat estimates between 40 m and 300 m. By indistinguishable, we mean that, using a hypothesis test based on the normal distribution, we fail to reject the hypothesis that the ensemble average of the 20 km bulk fluxes is equal to that of the 20 km eddy correlation fluxes with 90% certainty. Near the surface, the bulk sensible heat flux estimate is lower than the eddy estimate of the flux, while at the top of the mixed layer, the eddy correlation sensible heat flux is much smaller.

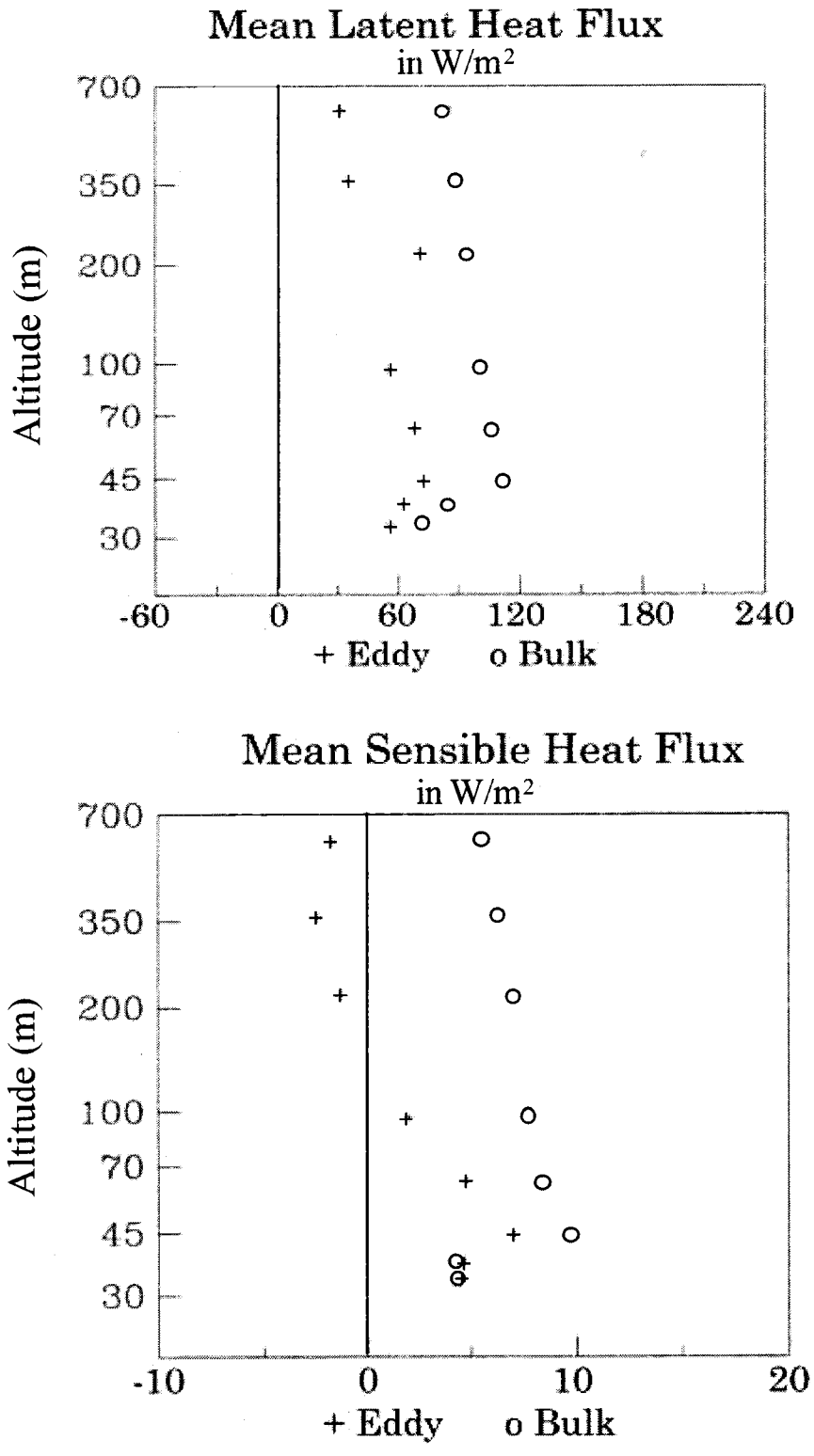

Figure 5.1: Variation of mean heat flux estimates (in W/m^2) with change in altitude.

A simple comparison between the eddy correlation estimate and the bulk estimate could also be made as follows:

$$\zeta = \frac{Bulk - Eddy}{\frac{1}{2}(Bulk + Eddy)} \tag{5.1}$$

Throughout this section, this "normalized deviation", ζ, will be simply referred to as the error of the flux. As discussed later in this chapter, this estimate of error is sensitive to small fluxes and may be large or indeterminate for those cases where the flux approaches zero.

The normalized deviation of the flux acts as an indicator of how well the eddy flux is estimated by the bulk aerodynamic formula. Over a range of heights, and if the bulk and eddy estimates are equal, the mean value of ζ will be zero. If the bulk flux estimate exceeds the eddy correlation estimate and the condition persists with height, then ζ will be positive and constant with height. Conversely, if the bulk estimate exceeds the eddy estimate, ζ will be negative with altitude (again assuming persistence with height). This is not to imply that ζ is dependent on height. Altitude dependence is seen as a height to height difference in this error measurement, its magnitude indicating the extent to which altitude affects the flux measurement method. We will see that the largest discrepancy between the bulk and eddy estimates occurs above the surface mixed layer (100 m) for sensible heat and is relatively constant for latent heat flux. This result is not surprising, since the similarity relationships used in the bulk flux algorithm are not valid outside of the surface layer (typically on the order of 100m). Below 100 m, the largest error occurs between 45 m and 70 m in both cases and averages +0.4% for sensible heat flux and +21% for latent heat flux within the surface layer. The result is slightly higher than that reported by Vickers and Esbensen (1998), but is not unreasonable. Vickers and Esbensen (1998) make a comparison of errors in Electra data based surface heat fluxes to those computed using R/V Moana Wave data and conclude that they are sufficiently equal for use in their subgrid analysis, but the

Electra bulk estimate of latent heat flux is consistently larger than buoy bulk flux estimates. This is an indication that the constant flux assumption in the surface layer is bad or that the Obhukov length over the analyzed flight legs is less than 100 m. Over the ocean in fair-weather conditions, the Obhukov length can be as small as 10m (Vickers and Esbensen (1998)).

Figure 5.2 shows the error in latent heat flux as a function of altitude. As is indicated by the positive error value, the bulk estimate tends to exceed the eddy estimate at all altitudes. Below 40 m, the bulk and eddy estimates appear to match each other very well. For the remainder of the surface layer (up to 100 m), error increases and can become as large as 5%. There is also increased variability in individual leg error (shown by the bars in Figure 5.2). Above 100 m, our estimate of error becomes more variable and approaches 10% or more. Again, this result is expected due to limitations on the validity of the bulk aerodynamic method above the surface layer.

In the sensible heat flux case (Figure 5.3), the bulk estimate is again consistently larger than the eddy estimate. In the surface layer (below 100 m), error reaches a maximum between 45 m and 70 m, but the uncertainty in our estimate of error increases significantly at 100m. Above the surface layer, there is significant variability in error on a leg by leg basis, but, on average, the error tends to be on the same order as that seen in the surface layer.

Other reasonable sources of error in heat flux computed by the bulk method include errors in the conversion from ambient temperature at aircraft level to that at sea level, where the fluxes are computed and errors in either sea-surface temperature measurement or ambient temperature measurement. It was shown that, for data taken aboard the Electra, there was an offset in air temperature that was not consistent from month to month (Burns et al. (1999)). A general offset of –0.6°C was applied to the air temperature data used in this study, but it was not adjusted on a flight-by-flight

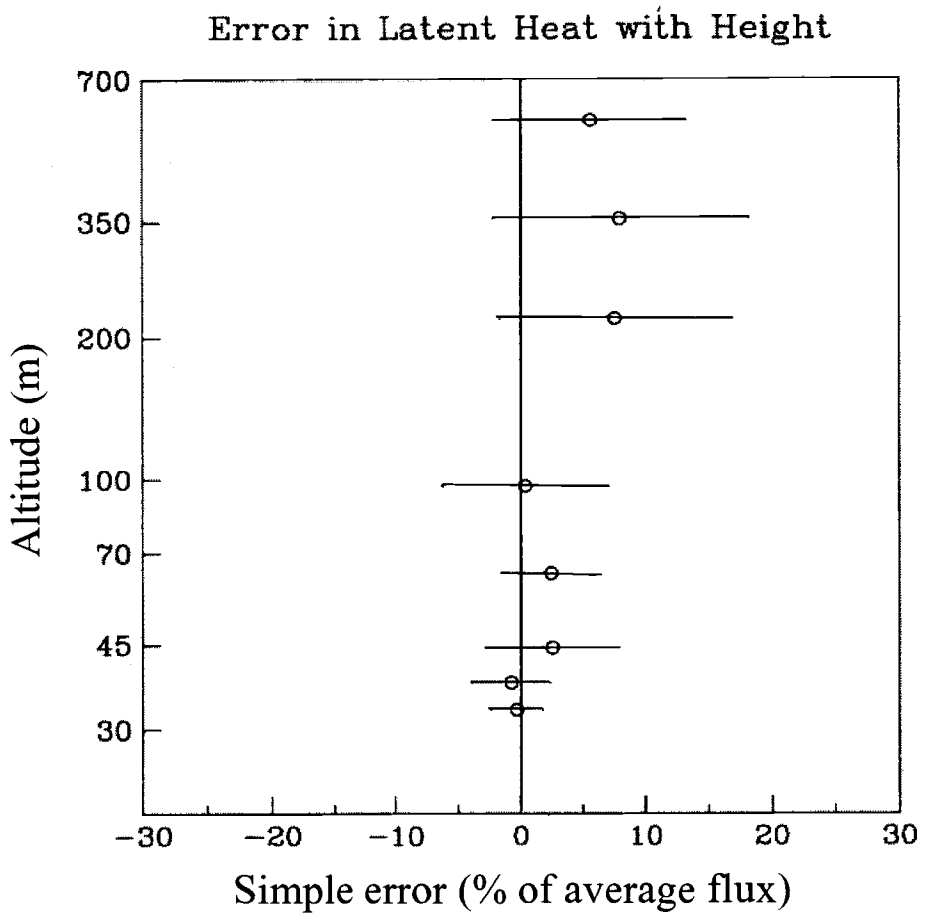

Figure 5.2: Variation with altitude of latent heat flux as a percent of the average of bulk and eddy estimates.

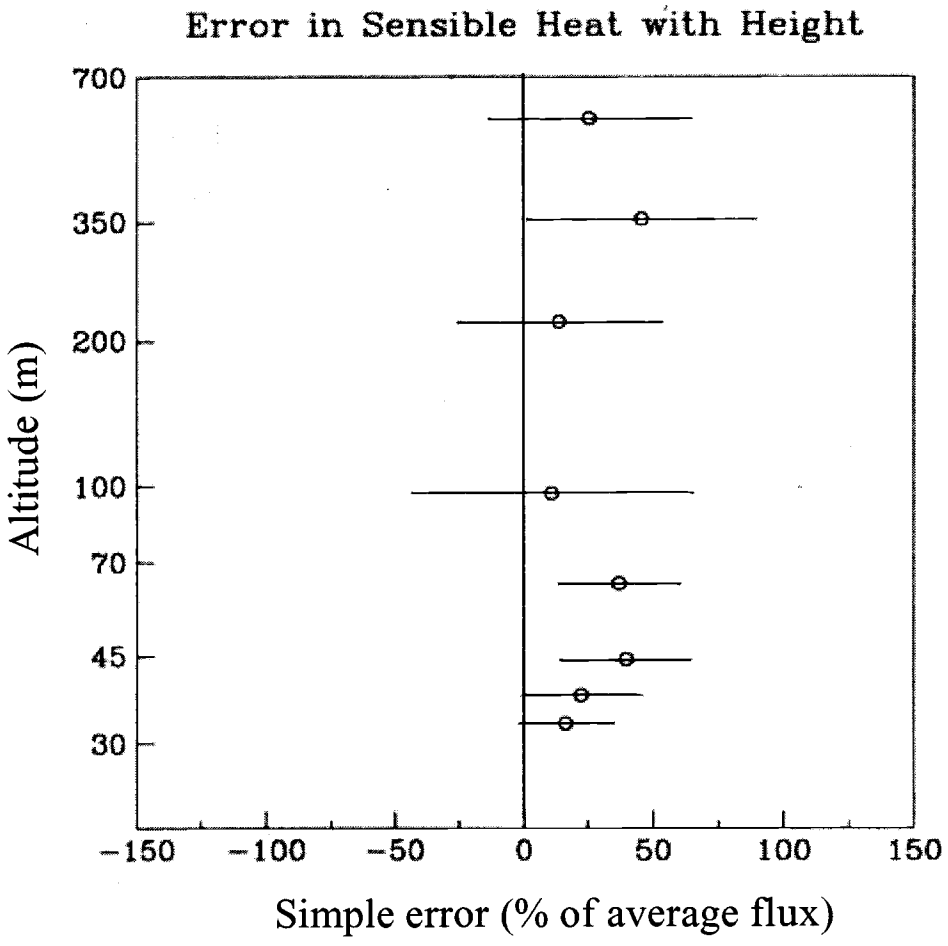

Figure 5.3: Variation with altitude of sensible heat flux as a percent of the average of bulk and eddy estimates.

basis. Errors in air-sea temperature difference can be a significant contributor to error in surface flux estimates (up to 10 W/m^2, Godfrey et al. (1996)).

It was also shown by Burns et al. (2000) that there is a small error in infrared sea surface temperature as a function of altitude, on the order of 0.25°C in the surface layer and about 0.5°C up to 400m. This correction would compensate for absorption at altitude and surface emissivity and could result in overestimation of the surface heat flux by up to 9% within the surface layer (linearly increasing from 0% error at the surface). Similarly, Sun and Mahrt (1995) find that the bulk aerodynamic method, using traditional similarity theory and surface radiative temperature, overestimates actual heat flux and that the problem is exacerbated in unstable conditions. However, because the error in Figures 5.2 and 5.3 is not a strong function of altitude (that is, since there is no linearly increasing trend in error with altitude) this type of error in surface temperature measurement is not believed to be the major contributor to the difference between the bulk estimate and the eddy correlation heat flux. It does, however, account for about 20% of the error shown at low altitudes (below 100m) in Figure 5.3. It should be noted, however, that the sea surface temperature is not corrected for cloud reflectance and Hagan et al. (1997) cite that these effects could result in further sea surface temperature error, and ultimately greater error in the estimate of the flux.

Finally, as alluded to previously, small Monin-Obhukov lengths over the ocean could also mean that Monin-Obhukov similarity theory simply would not apply. Outside of the surface layer, temperature and humidity profiles may be influenced by processes that Monin-Obhukov similarity theory does not include.

The bias in latent heat flux computed by the bulk aerodynamic method relative to that computed by eddy correlation is illustrated in Figure 5.4. As the magnitude of flux increases, the bias seems to increase as well, with the lower magnitudes (less than 55 W/m^2 by the eddy estimate) conforming to a 1:1 slope and with higher magnitudes transitioning to a slope closer to 5:3.

Similarly, the correlation between bulk and eddy sensible heat flux is shown in Figure 5.5. The two estimates are well correlated in the 0 W/m^2 to 7.5 W/m^2 region (as computed by eddy correlation). As eddy correlation predicts negative heat flux, however, the bulk method tends to hover near zero. Above 7.5 W/m^2, the bulk method is again biased high relative the eddy correlation and there is considerable scatter in the data.

Fairall et al. (1996) used R/V Moana Wave measurements made during TOGA COARE to determine empirically adjustable parameters in the COARE algorithm for the Charnock and gustiness formulations. The resulting correlation between flux covariances and bulk flux estimates of latent and sensible heat flux was "remarkable" (Fairall et al. (1996)) with little scatter. However, when Electra data was used to compute bulk fluxes and compared to the corresponding eddy correlation values, the result was too scattered to draw any meaningful conclusions about the algorithm's accuracy. The comparison made by Fairall et al. (1996) using Electra data uses weak wind data, so the range of fluxes is somewhat smaller than that in Figures 5.4 and 5.5. However, the analysis presented by Fairall et al. (1996) reveals somewhat more scatter in comparison of both latent heat fluxes and sensible heat fluxes than the weak wind data presented here.

Greischar and Stull (1999), Vickers and Esbensen (1998), and Khelif et al. (1997) compare direct measurement of latent and sensible heat flux from aircraft to fluxes predicted by the COARE algorithm. The analysis of Greischar and Stull (1999) consists of 25 low altitude (<66 m) Electra flight legs with wind speeds between 0.8 m/s and 7.8 m/s. In this analysis, the COARE algorithm overpredicts both sensible heat flux and latent heat flux, with errors being greatest for wind speeds above 5 m/s. Agreement is best in Greischar and Stull's (1999) analysis for sensible heat flux at low wind speeds. Vickers and Esbensen (1998) show the same trends with wind speed in comparing low-level Electra sensible and latent heat fluxes. These trends are consistent with those shown in Figures 5.4 and 5.5. Vickers and Esbensen (1998) consider that the difference between the bulk flux estimate and the eddy correlation flux possibly

arises from (1) flights nearly always being outside the boundary layer, (2) potential fundamental differences between buoy and aircraft measurements, and (3) the possibility of unresolved instrumentation or calibration problems on any of the platforms, but they conclude that the fluxes agree well enough to complete their analysis.

Using WP-3 data, Khelif et al. (1997) show that eddy correlation latent heat flux from aircraft data is on average 20 W/m2 less than that predicted by the COARE algorithm. In the case of sensible heat, the means are not statistically different (meaning that there is no bias between eddy correlation flux and the bulk estimate of the flux), but there is a large amount of scatter between the estimates. There is also relatively poor agreement between the eddy correlation fluxes measured on the aircraft and those measured on the Moana Wave. This is a possible indication that one source of error is that the characteristic of the flux at altitude is different from that at the surface. In Khelif et al. (1997), errors in sea surface temperature measurement are also cited as a possible cause of the bias.

Other comparisons of the bulk flux estimate and eddy correlation flux for both sensible and latent heats have been made using shipboard data (Bradley et al. (1996), Song et al. (1996), and Chang and Grossman (1999)). Chang and Grossman (1999) use R/V Moana Wave data and, as expected based on Fairall et al. (1996), find good agreement between the two methods of flux calculation. Song et al. (1996), however, use measurements from the R/V Kexue and find that the eddy correlation latent heat flux is systematically lower than that predicted using the COARE algorithm. This result is not definitively resolved in Song et al. (1996), but inaccuracy in wind measurement is cited as a possible cause for the discrepancy.

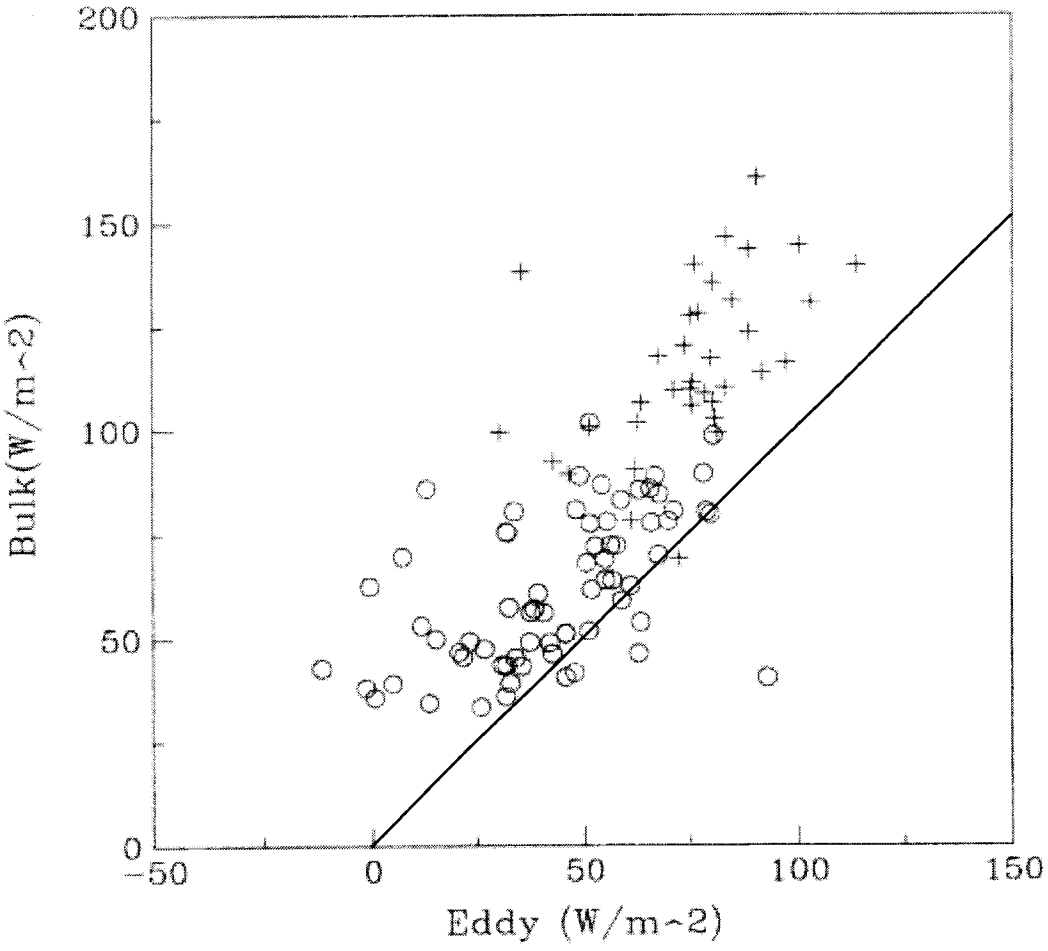

Figure 5.4: Comparison of eddy correlation results to bulk aerodynamic method results for latent heat flux. Plusses indicate strong wind and circles indicate weak wind flight legs.

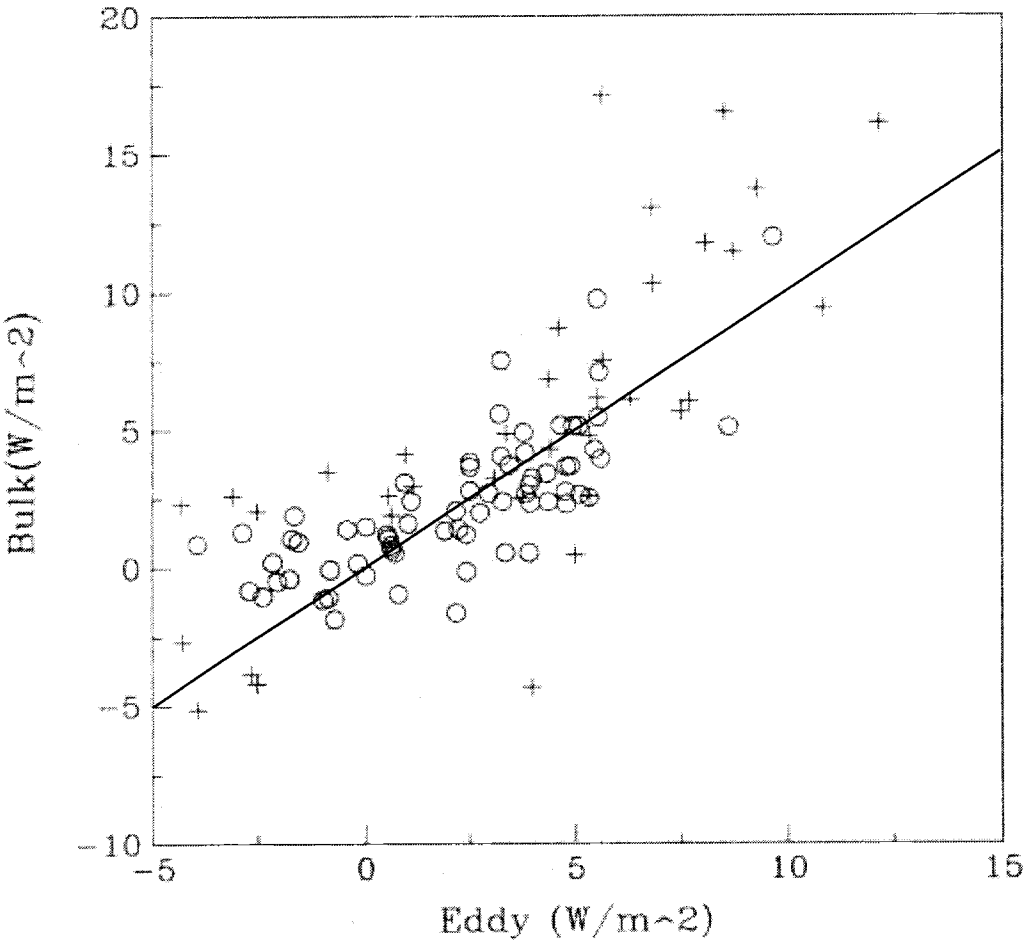

Figure 5.5: Comparison of eddy correlation results to bulk aerodynamic method results for sensible heat flux. Plusses indicate strong wind and circles indicate weak wind flight legs.

5.2 Errors introduced by averaging

As mentioned previously, the bulk aerodynamic method is based on the premise that, given equilibrium conditions and that the surface layer is a constant flux layer, fluxes may be reasonably represented as follows:

$$E = \rho L_v \overline{w'q'} = \rho C_E \overline{U}\left(q - q_{sfc}\right)$$
$$H = \rho C_p \overline{w'q'} = \rho C_H \overline{U}\left(T - T_{sfc}\right) \tag{5.2}$$

where E indicates latent heat flux and H indicates sensible heat flux. Each of the components of Equation 5.2, U, q, and T, are locally averaged values. For example, with buoy data, these may be hourly averages. In the case of aircraft data, they would be spatial averages representing a similar scale. There is no real question to the method of averaging q and T -- they are scalars and ensemble averaging makes the most sense. Velocity, however, is a vector and we are therefore faced with a choice: to use the vector average or the scalar average. The implications of this choice are investigated in this section.

Conventionally, the bulk method for calculating sensible and latent heat flux uses the scalar averaged wind speed. The scalar averaged wind speed is more representative of the wind in the sense that changes in direction do not work to decrease the estimated magnitude of the wind. Furthermore, in GCM's, the effect of variability in wind speed and direction below the scale of the model is not resolved. The bulk method has proven to be adequate at middle and subtropical latitudes where the vector and scalar windspeeds are not too different. Discrepancies may arise, however, between vector and scalar windspeeds in the weak wind or gusty situations typical of the western Pacific warm pool. In this case, the vector average may be much larger than the scalar average. Therefore, the resulting fluxes will show similar disagreement. This begs several important questions: (1) how drastic is the effect of this difference in windspeed estimate on the estimate of the flux, (2) what effect does

local averaging method have on the flux estimate, and (3) is the effect the same for large scale averaging of the windspeed.

Apparently contradictory statements in previous studies lead us to hypothesize that this effect is small. Several scientists have observed regions of enhanced evaporation associated with mesoscale systems. Johnson and Nicholls (1983) observe a marked increase in evaporation behind a squall line and Young et al. (1992) noted similar, although less dramatic, increases in evaporation with systems in the warm pool region. Existing climatologies, however, seem to indicate that these regions of deep convection do not represent long term global average maxima of evaporation. On the contrary, evaporation near the equator appears to be smaller over the long term than that in the trade wind zones (Esbensen & Kushnir (1981)). If all of these observations are true, the only logical conclusion is that the local (short-term) enhancement of evaporation associated with deep convection is either not large enough or not persistent enough to have a large effect on the average flux.

Esbensen and McPhaden (1996) look at the difference between the vector averaged and total fluxes as the "mesoscale enhancement" of the flux. As the wind speed decreases, the contribution mesoscale motions to the local flux becomes more apparent. As motion increases, the local mesoscale contribution begins to vanish. Using data from the TOGA TAO buoy array, they showed that over monthly-averaged periods, the mesoscale enhancement of surface fluxes is small (less than 10% of the total flux) and vector average flux explains most of the flux over the tropical Pacific. This would appear to be the case with aircraft data as well.

Vickers and Esbensen (1998) estimated the subgrid enhancement of evaporation and sensible heat flux from one-dimensional aircraft data in fair weather TOGA COARE conditions. Results pertinent to subgrid flux enhancement obtained in this study are discussed later in this section.

5.2.1 Aircraft versus buoy measurement

The analysis done by Esbensen and McPhaden (1996) forms the basis for the work done in this section. Esbensen and McPhaden (1996) use buoy data for their analysis. It is therefore instructive to consider the validity of transferring their method from buoy measurements to aircraft data. The conceptual differences between aircraft and buoy measurements are discussed here and are followed by the argument that the calculations are in fact comparable.

The TOGA TAO buoy array provides one view of the climatology in the tropics. Buoys provide hourly averaged meteorological information about windspeed and direction, temperature, and humidity as well as information about the state of the ocean (temperature, salinity, etc.). Buoys, however, are passive observers. That is they measure only the events that happen to advect past their location. Additionally, they are only capable of near surface measurements.

Aircraft have the ability to sample at various altitudes (concurrently if more than one aircraft is used) and in various directions relative to the propagation of a system. Another major advantage is that the aircraft are capable of sampling almost continuously in space over a variety of conditions, including transecting convective systems. The TAO array is distributed over the tropical Pacific, but they are spaced too far apart (~10 degrees east to west) to resolve short-lived mesoscale effects. This spacing is most useful in examining intraseasonal to interannual variability on large spatial scales. With the aircraft, temporal resolution is lost. There are other disadvantages to aircraft data as well. There may be sampling errors introduced in three ways: (1) due to the finite nature of the leg, (2) due to the empirical nature of the similarity profile functions used in translating measured fluxes to the surface (as well as uncertainties in computation of bulk exchange coefficients), and (3) due to warming or cooling of the sensors as altitude changes.

Overall and depending on what type of information is desired, it can be said that either method is adequate. Buoy data is useful in investigating long term changes in surface conditions and in evaluating interactions between the atmosphere and ocean at a point in space. In the case of the TAO array, buoys are useful in simultaneously sampling conditions over a range of locations as well. Aircraft data are more useful in observations of specific systems. of smaller scale circulations, and at several altitudes.

Usefulness of a method does not define its limits of usefulness, though. Flux calculations rely on the prudent choice of averaging length, not solely on the method of measurement. Because strict ensemble averaging is not practical in a meteorological context, we are forced to settle for temporal or spatial averages as acceptable substitutes assuming the flow is stationary. If the flow is in equilibrium (implied by stationarity), the relative motion of the instrument becomes important rather than changes in its position. The averaged fluxes will provide essentially the same information on a given set of fluxes as long as the temporal scale of the buoy-derived fluxes is comparable to the spatial scale of the aircraft-derived fluxes when either is placed in context. Averaging lengths in this chapter have been chosen accordingly.

The choice of large scale averaging length, λ, is equally arbitrary but with less well-defined physical constraints. The ultimate goal is to sample mesoscale and larger motions, but with aircraft data the distance over which satisfactory measurements are taken is limited. Ideally, a distance greater than 150 km would correspond to the daily average used by Esbensen & McPhaden (1996). Statistically, however, there are not enough straight, continuous, homogeneous records of that length to ensure reliable results. As a compromise between idealism and the reality of the statistics, a minimum record length of 50 km was chosen resulting in approximately half of the flight legs satisfying all of the criteria. This record length is assumed to be large enough to sample several mesoscale eddies. Thus it is assumed that there is no bias introduced by sampling too few mesoscale motions.

As a check, latent and sensible heat flux computed from 50 km record lengths is compared to that computed from 75 km record lengths. When compared to the 75 km records, the difference in flux is not significant (Table 5.1). For all qualifying legs, latent heat flux is 85 W/m^2 in the 50 km cases and 82 W/m^2 in the 75 km cases, a 4% difference in means with statistically indistinguishable populations. Similarly, sensible latent heat flux is 3.55 W/m^2 in the 50 km cases and 3.54 W/m^2 in the 75 km cases, with statistically indistinguishable populations.

5.2.2 Mesoscale flux enhancement

The overall ensemble properties of the fluxes are presented in Table 5.1. These fluxes are small compared to the result in Esbensen and McPhaden (1996), but evaporation estimates agree well with published results obtained for TOGA COARE (Vickers and Esbensen (1998)). For all of the flight legs, winds are light (less than 10 m/s and averaging about 3 m/s) and buoyancy effects become important. We would thus expect transport to be dominated by convection. The increase in latent heat flux with increased wind speed is consistent with previous observations of increased flux with increased wind speed (Esbensen and McPhaden (1996)).

		Latent Heat Flux			Sensible Heat Flux		
L	Wind	Mean	Std. Dev.	# Obs.	Mean	Std. Dev.	# Obs
50 km	all	85.16	34.68	108	3.55	4.19	108
50 km	>4 m/s	122.5	21.90	39	5.29	5.79	39
50 km	<4 m/s	64.06	19.33	69	2.56	2.46	69
75 km	all	81.68	30.58	49	3.54	3.90	49

Table 5.1: Dependence of total flux on wind and averaging length. Fluxes are listed in W/m^2.

Table 5.2(a) lists the mesoscale enhancement as a fraction of total flux averaged over all legs. When winds are less than 4 m/s, mesoscale enhancement accounts for up to 5% of the total latent heat flux and almost 1% of the sensible heat

flux. Above 4 m/s, the mesoscale enhancement is significantly smaller in the latent heat flux case, but becomes relatively large for sensible heat. This result contradicts both Esbensen and McPhaden (1996) and Vickers and Esbensen (1998) for the sensible heat case, but is otherwise consistent. The discrepancy is due to one outlier in the population of computed mesoscale enhancement. For one flight leg, the computed mesoscale enhancement was greater than 100% (that is, larger than is physically reasonable). Values in parentheses in Table 5.2 represent the population with the outlier removed. With this refined population, the sensible heat flux mesoscale ehnancement trends match those shown in Esbensen and McPhaden (1996) and Vickers and Esbensen (1998). Percentagewise, the mesoscale enhancement of sensible heat flux in this study is close to that reported by Vickers and Esbensen (1998), but smaller than that in Esbensen and McPhaden (1996).

(a)	$\Delta E/\langle E\rangle$ %	ΔE W/m^2	$\Delta H/\langle H\rangle$ %	ΔH W/m^2
>4 m/s	1.49	1.82	2.02	0.11
<4 m/s	5.40	3.46	0.94 (7.44)	0.02

(b)	$\Delta Es/\langle E\rangle$ %	ΔEs W/m^2	$\Delta Hs/\langle H\rangle$ %	ΔHs W/m^2
>4 m/s	0.06	0.074	0.62	0.033
<4 m/s	-0.31	-0.020	-5.15 (1.99)	0.013

Table 5.2: Mesoscale flux enhancement (a) and gustiness effect (b) in light and strong winds. Values in parentheses indicate sensible heat mesoscale enhancement population with outliers removed (see text for details).

From Table 5.2(b), it is clear that the light wind case is more readily affected by gustiness. $\Delta E_s/\langle E\rangle$ and $\Delta H_s/\langle H\rangle$ represent error 'introduced' by using a scalar averaged wind speed rather than vector-averaged wind, and can therefore be attributed to gustiness. Although the contribution of gustiness to overall flux is small in the latent heat case, the light wind error is 5 times that in strong winds. In the sensible

heat case (with a population filtered for outliers), the mesoscale enhancement in strong winds is one-third of that in weak winds.

The corrected results in Table 5.2 are consistent with Esbensen and McPhaden (1996) and Vickers and Esbensen (1998). However, sensible heat enhancement estimates are slightly smaller than those found by Vickers and Esbensen (1998) for a similar set of data (percentage-wise, 9% and 11% in Vickers and Esbensen (1998) vs. 2% and 8% in this study for latent heat flux enhancement and sensible heat flux enhancement, respectively). This is likely an artifact of choice of averaging length (or grid-box size in Vickers and Esbensen (1998)). Redelsperger et al (2000) look at meosocale enhancement by gustiness and by precipitating convection. In that study, sensible heat flux is 20 W/m^2 with enhancement of 5 W/m^2 and latent heat flux is 120 W/m^2 with mesoscale enhancement of 25 W/m^2. On a percentage basis (25% in Redelsperger et al (2000) vs. 5% in this study for sensible heat and 20% vs. 2% for latent heat), this result exceeds the estimates of mesoscale flux enhancement in this study, but the flight legs included here are computed for fair-weather conditions over a variety of flight legs. There have been several other TOGA COARE case studies examined in a similar context with similar results (Saxen and Rutledge (1998) and Williams (2001)).

Figures 5.6 and 5.7 show the data for all applicable flights with strong and light wind speeds, respectively. Again, the enhancement curves for the strong wind case are relatively flat and uninteresting, but in the weak wind case there is considerable variability. One may notice that in the weak wind case the magnitude of the fluxes is suppressed.

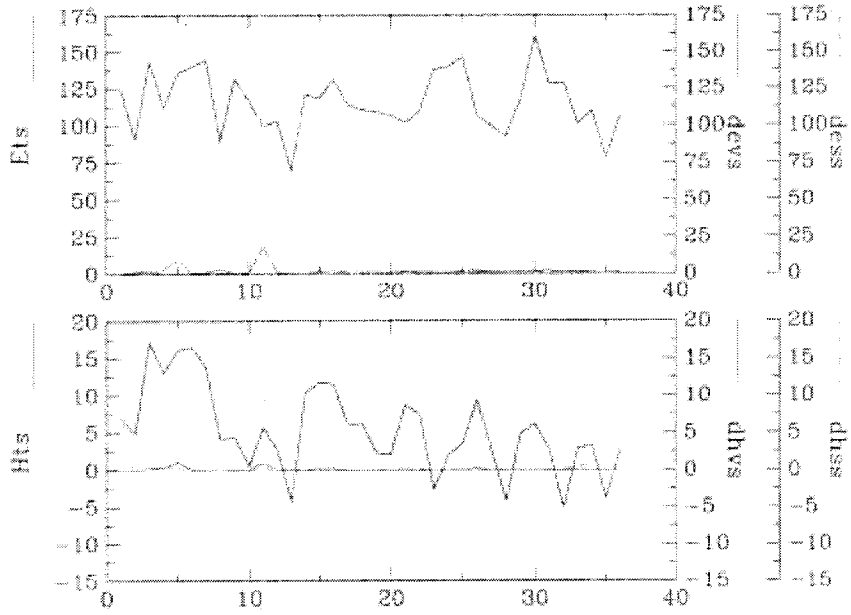

Figure 5.6: Variation of total latent heat flux (Ets) and total sensible heat flux (Hts) in the strong wind case. The series labeled dess, devs, dhss, and dhvs represent the deviation from the total flux to the scalar (s) and vector-averaged (v) latent (e) and sensible (h) heat fluxes, respectively.

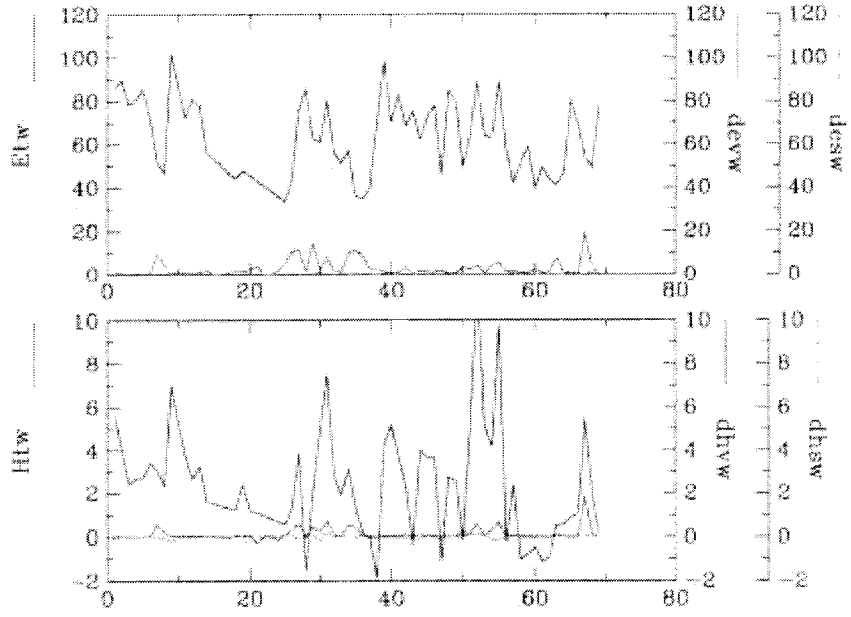

Figure 5.7: Variation of total latent heat flux (Etw) and total sensible heat flux (Htw) in the weak wind case.

Figures 5.8 and 5.9 illustrate the clear separation between fluxes in the weak wind and strong wind cases. Evaporation is suppressed in the weak wind case and becomes more variable with strong winds. The suppression may be due to lack of efficiency of convective transport processes compared to that of the advective processes. That is, the convection dominates the transport in the weak wind case, but there is no real means of transport of drier air into the region. Figures 5.7 and 5.8 reveal similarity in the magnitudes of the vector-averaged evaporation and the total evaporation. This is indicative of the small effect of wind variability on the overall flux estimate and is consistent with Esbensen and McPhaden (1996) and with Vickers and Esbensen (1998). Sensible heat flux appears to have a somewhat opposite characteristic. Its magnitude does not appear to depend strongly on wind speed, however scatter increases dramatically with wind. The increased scatter may be due air masses of different properties advecting into the region. There is no preference as to sign because high wind speeds do not indicate a region of temperatures that is discrete from that in light wind conditions.

Figure 5.10 shows the relationship between the mesoscale enhancement of latent heat flux and that of sensible heat flux, with the plusses representing the strong wind case and the circles representing and weak winds. Overall, there is a clear correlation between the latent and sensible heat flux estimates. The sensible heat flux enhancement appears to be systematically higher than the latent heat flux enhancement. This result is consistent with that published by Esbensen and McPhaden (1996).

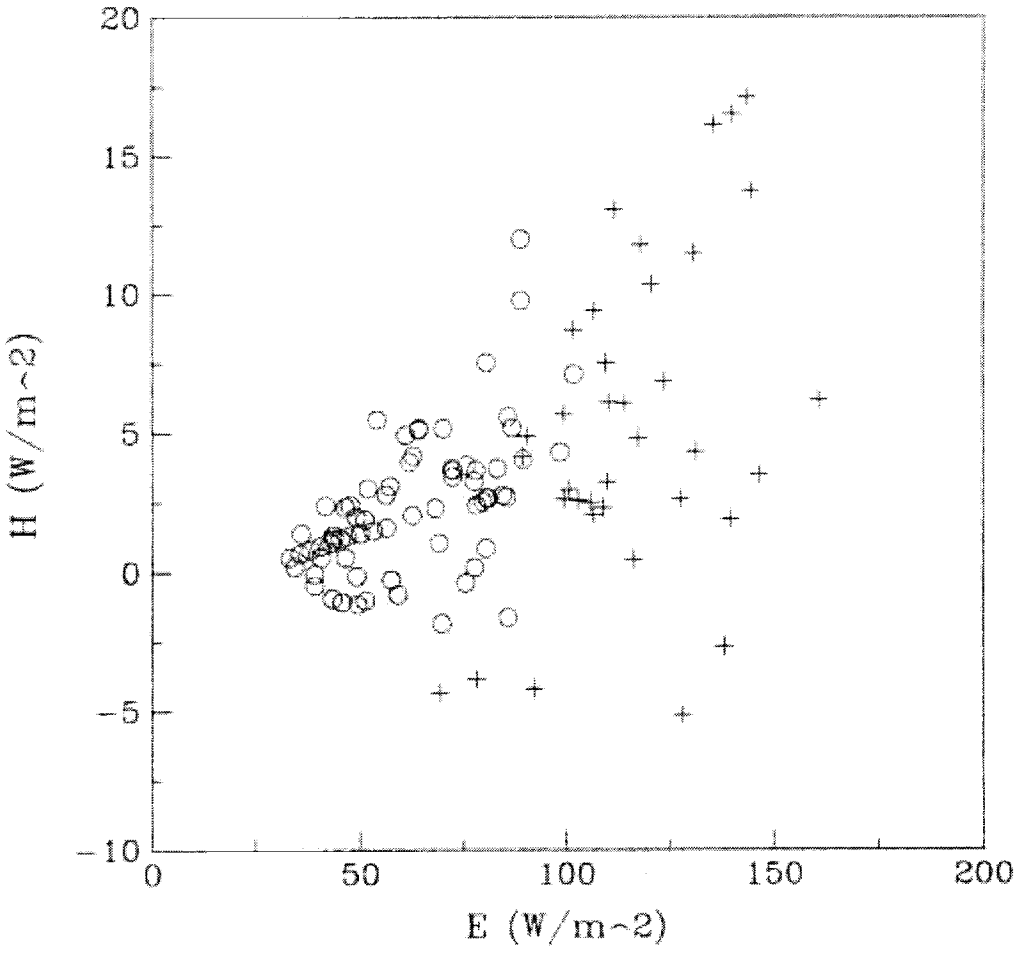

Figure 5.8: Comparison of total sensible heat flux to total latent heat flux for all flight legs. Circles represent the weak wind (<4 m/s average) case and plusses represent strong winds (> 4 m/s).

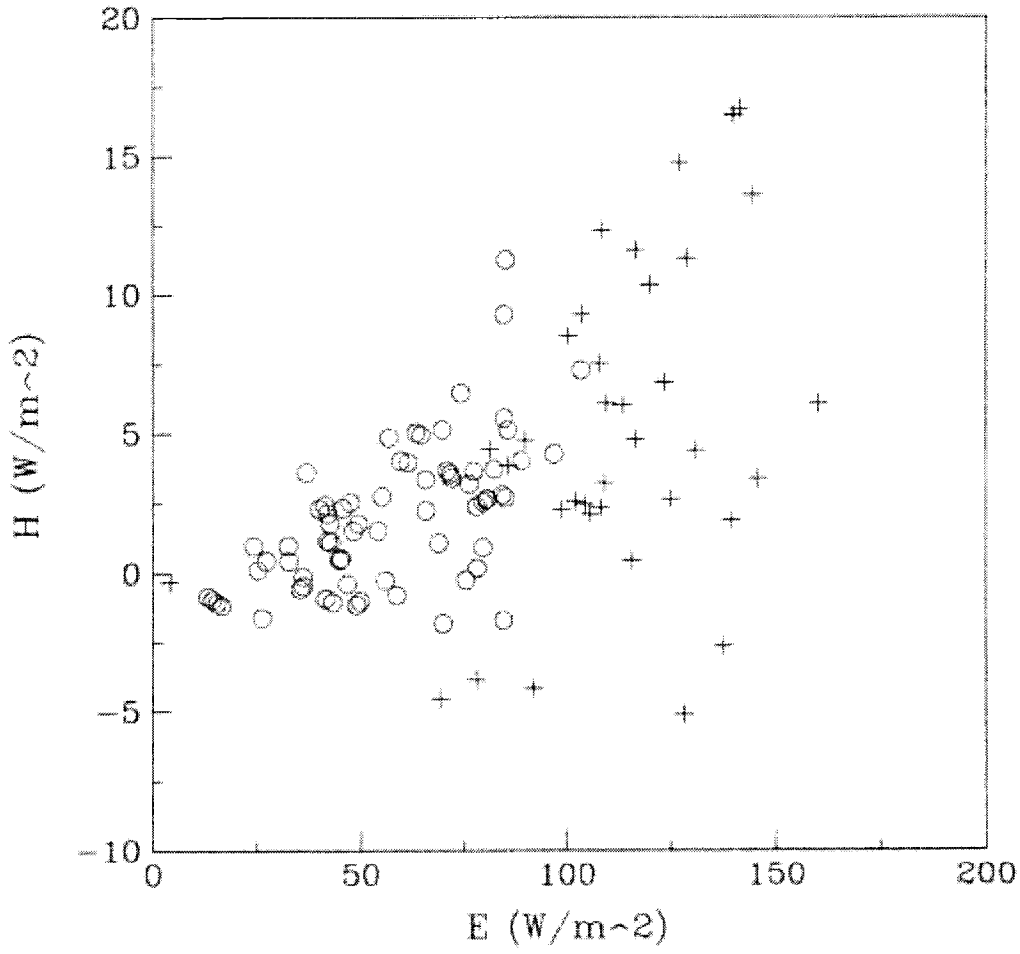

Figure 5.9: Comparison of vector-averaged heat fluxes for all flight legs. Circles represent the weak wind case and plusses represent strong winds.

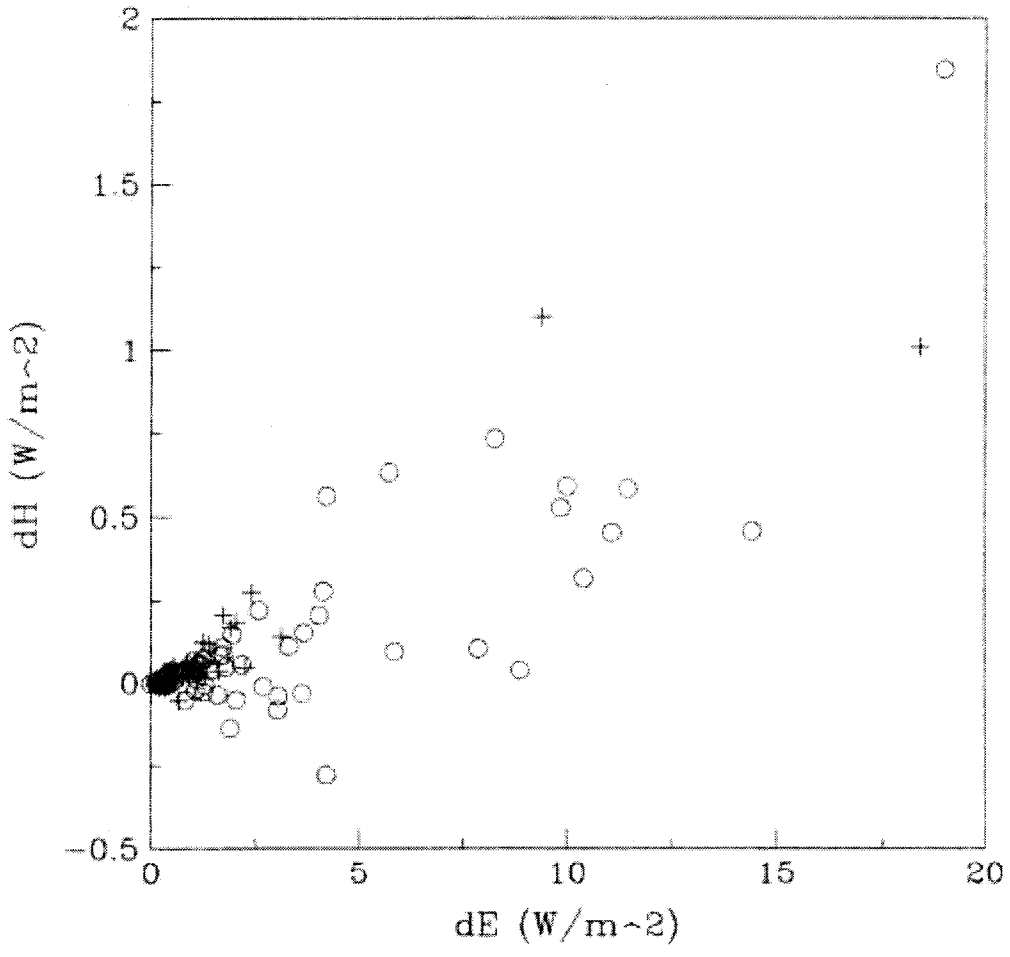

Figure 5.10: Comparison between sensible heat mesoscale flux enhancement and latent heat mesoscale flux enhancement. Circles represent the weak wind case and plusses represent strong winds.

6. Month by Month Comparisons

Sensible heat and latent heat estimates are correlated for total and vector fluxes for each month during the TOGA COARE observation period. It will be shown that, for all altitudes, the difference is consistent from month to month and that there is a weak correlation between the two flux estimates in light winds and a stronger correlation in strong winds. This supports the argument that sensible and latent heat estimates are not easily separated (Sun et al. (1995)).

This chapter also compares bulk and eddy flux estimates to one another on a month-by-month basis. As was seen in chapter 5, the bulk estimate is biased high relative to the eddy estimate and there is significant scatter in all months. This indicates that, in addition to the corrections for gustiness and sea-surface temperature, significant averaging is necessary for the bulk method to be a reasonable predictor of the eddy flux.

6.1 Flight conditions

The distributions of flight leg properties between November, December, and January vary somewhat. Ambient temperature, sea surface temperature, and humidity tend to be consistent month to month. Ambient temperature is consistently 26-29°C in flights below 90 m and decreases logarithmically above 90m from 28°C at 90 m to 22°C at 1000m. Humidity remains constant up to 500 m, at which point it begins to decrease slightly from 175. G/kg at 500 m to 14.5 g/kg at 1000 m. There are however, some interesting trends to note in the distribution of altitude month to month (Tables 6.1& 6.2) and in wind speed variation (Table 6.1). This distribution of altitude, in conjunction with variation in horizontal wind speed, allows for some analysis of the accuracy of flux estimates as a function of altitude and wind.

Month	Number of flight legs	altitude (m)			horizontal wind speed (m/sec)		
		min	median	max	min	median	max
November	22	31	43	66	1.7	3.8	6.5
December	75	33	94	989	0.4	2.8	6.8
January	71	29	96	954	0.6	3.3	9.2

Table 6.1: Average flight statistics by month.

Month	Surface layer (SL)	SL to ML Transition	Mixed layer (ML)	Entrainment zone	Above boundary layer
altitude range	0m to 40m	40m to 70m	70m to 300m	300m to 800m	above 800m
November	45%	55%	0%	0%	0%
December	41%	8%	17%	28%	5%
January	39%	7%	24%	28%	1%

Table 6.2: Distribution of flights by altitude and month. Altitudes are based on Stull (1998).

6.2 Total vs. vector averaged bulk flux

Overall, November included only flights below 70 m, with a median altitude of 43 m and a median wind speed of 3.8 m/s. December and January included a similar number of surface layer/lower mixed layer flights to November, but there were several higher altitude flights as well. In these two months, the flights covered the entire boundary layer, with median altitudes of 94 m and 96 m, respectively. Winds in December tended to be slightly calmer than in November, but not significantly. It should be noted that the majority of strong wind cases (> 4 m/s) in December occur

below 100 m while in January, there are significantly more high altitude strong wind flight legs.

November fluxes consist solely of low altitude flights. When comparing sensible and latent heat flux (Figures 6.1 a & b) we see a couple of things. First, the sensible heat flux is never negative, indicating upward mixing. Second, weak wind fluxes are consistently and systematically smaller than those in strong winds (39% smaller for latent heat flux and 70% smaller for sensible heat flux, see Table 6.3). There is a correlation between sensible and latent heat where, for every 10 W/m^2 increase in latent heat flux, there is a 1.6 W/m^2 increase in sensible heat flux (Table 6.4) and the estimates are well-correlated. Vector averaged and total heat flux show similar slopes with a similar increase in scatter at higher wind speeds.

	Average Latent Heat Flux			Average Sensible Heat Flux		
	>4 m/s	<4 m/s	all	>4 m/s	<4 m/s	All
Nov	127	78	95	12.7	3.8	6.9
Dec	110	60	69	5.6	2.1	3
Jan	125	63	93	3.5	2.9	3.2

Table 6.3: Average total heat fluxes month by month

	Slope			Correlation		
	>4 m/s	<4 m/s	all	>4 m/s	<4 m/s	All
Nov	0.195	0.062	0.163	0.8	0.6	0.9
Dec	0.189	0.053	0.071	0.7	0.6	0.7
Jan	N/A	0.109	N/A	0	0.5	0.2

Table 6.4: Summary statistics for correlation of sensible heat bulk flux estimates to latent heat bulk flux estimates.

During December (Figure 6.2), we begin to see negative sensible heat flux, particularly in the weak wind cases. This negative flux is indicative of downward mixing, most likely in high altitude flights. Neglecting those points for a moment, we note that the scatter in positive fluxes is similar to that seen in November flights. Weak wind fluxes also appear to be linearly related, though with a much smaller slope (for every 10 W/m^2 that latent heat flux increases, sensible heat flux increases only 0.71 W/m^2). Again, we note that fluxes are significantly smaller in weak winds that in strong winds (45% less for latent heat flux and 63% less for sensible heat flux, neglecting negative data points, see Table 6.3). As in November, average and total fluxes again show similar trends with similar increase in scatter at higher wind speeds and flux. It is difficult to draw a conclusion about the negative flux dependence on wind speed during December flights, since there are few relevant data points.

Because the change in flux appears to happen December and worsen in January, and because there is an increasing number of high altitude flights between November and January, it would appear that the trend is, at least in part, due to the inclusion of these high altitude flight legs. This could be a testament to the weakness of the similarity relationships or a warning that the bulk method, as it appears in the COARE algorithm may lose some merit near the top of the atmospheric boundary layer. It should be noted that the suspicious points do not appear to show any preference to location relative to the boundary layer.

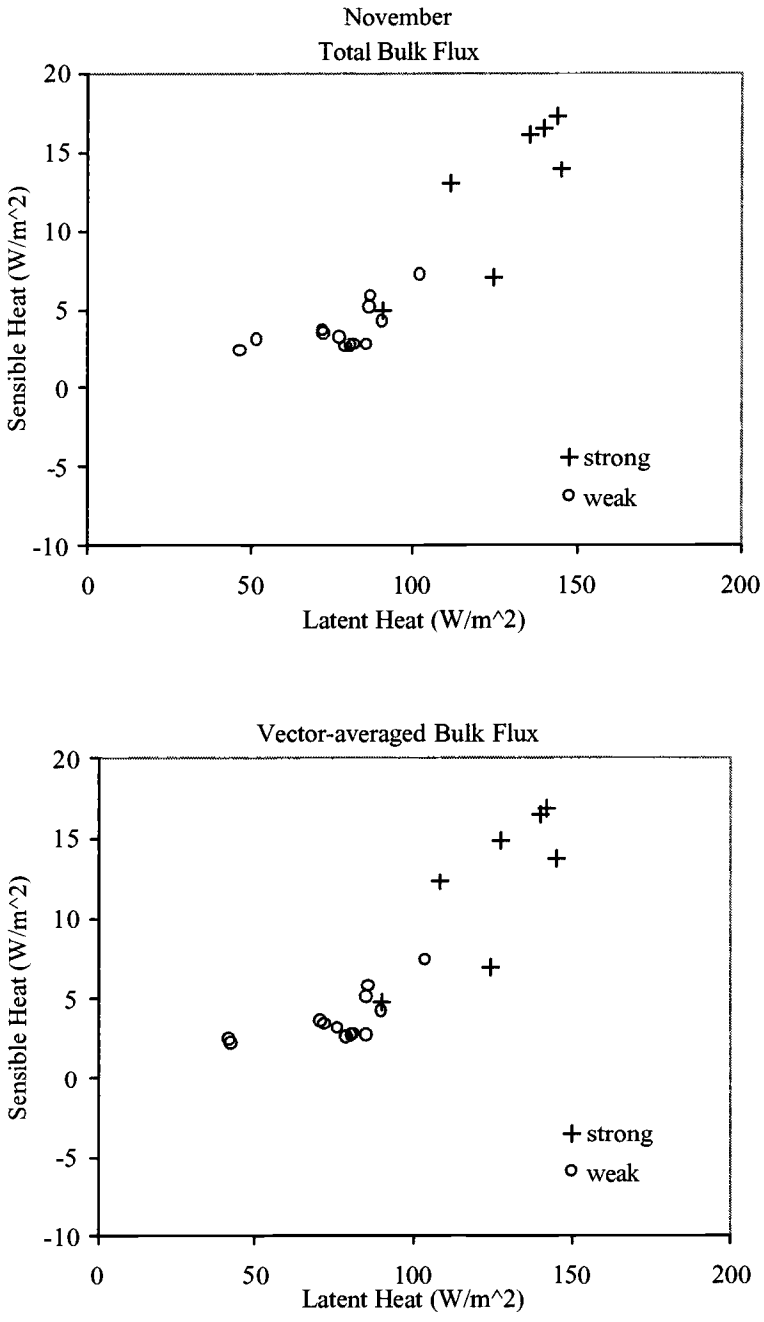

Figure 6.1: Month by month total flux & vector averaged flux, November

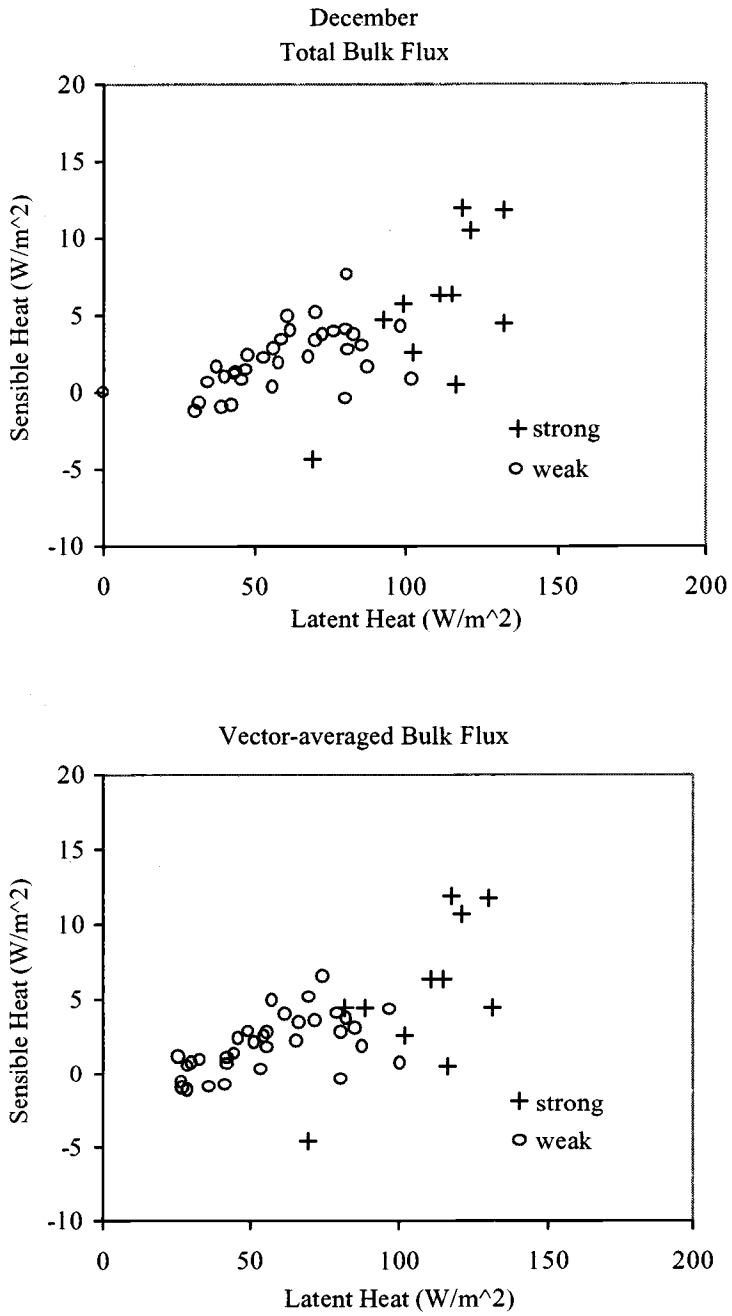

Figure 6.2: Month by month total flux & vector averaged flux, December

January exhibits much more flux variability with wind speed (Figure 6.3). There are more flights with negative latent heat flux and with corresponding stronger winds. In positive latent heat flux cases, however, there is no clear correlation of sensible to latent heat flux (Table 6.4). There is as much variability in weak wind sensible heat as there is in strong winds, but the latent heat estimates are still consistently less in weak wind cases (50%). For negative flux cases, stronger wind tends to drive sensible heat more negative while increasing latent heat. That is, for a 10 W/m^2 increase in latent heat flux, sensible heat flux decreases by 0.5 W/m^2. In a manner consistent with the previous months, total and vector-averaged bulk fluxes exhibit trends consistent with one another.

The changes in correlation between sensible and latent heat bulk flux estimates from month to month can be attributed to variability in flight conditions, specifically in altitude and wind speed. For low altitude flights, there appears to be a strong relationship between sensible and latent heat flux and vertical wind speed (with much more variability in strong winds). As higher altitude cases are included, this correlation still holds up for weak winds, although latent heat estimates appear suppressed relative to sensible heat. Finally, at high altitudes (those where sensible heat flux becomes negative), there is a decreasing trend in sensible heat flux as latent heat flux increases and it does correspond with increasing wind speed.

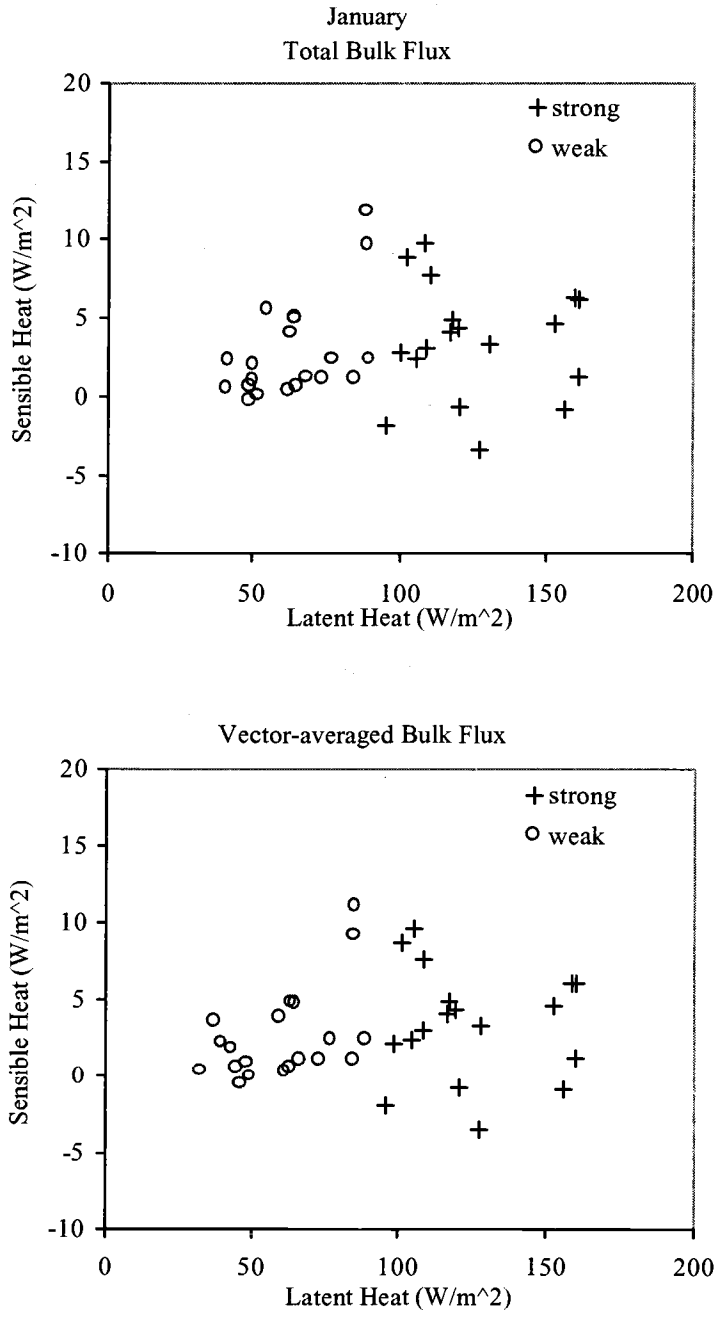

Figure 6.3: Month by month total flux & vector averaged flux, January

6.3 Eddy and bulk flux comparison

A comparison between the eddy and bulk estimates of latent and sensible heat reveals that there may be some problems in one of the methods. In the weak wind case, there is little or no bias in either latent of sensible heat suggesting that the gustiness factor does an adequate job of correcting for the singularity in the similarity relationships as wind speed approaches zero. In strong wind cases, however, the bulk method clearly overestimates the eddy correlation flux. That is, in the sensible and latent heat fluxes respectively the bulk estimate tends to be ~2 W/m^2 and ~10 W/m^2 higher than the eddy correlation estimate.

A breakdown by month similar to that done earlier in this chapter reveals that the eddy fluxes tend to be smaller than the bulk fluxes in December and January. This change is believed to be attributable to the inclusion of higher altitude flights as well.

6.3.1 Latent heat

Bulk estimates of latent heat flux are compared to eddy correlation fluxes in Figure 6.4. As in the previous analysis, the data is split out by month, Figure 6.4a being all legs in November, 6.4b in December, and 6.4c in January.

In the case of latent heat, strong wind fluxes are consistently higher than eddy fluxes and the bulk estimates are consistently higher than the eddy correlation flux values (that is, the bulk method tends to over-predict the eddy correlation flux in all months). The correlation in all months has a large amount of scatter as well. This indicates that there is not a correlation between the bulk estimate of the flux and eddy correlation flux on a leg-by-leg basis. There is no apparent relationship between scatter and wind speed or flight altitude.

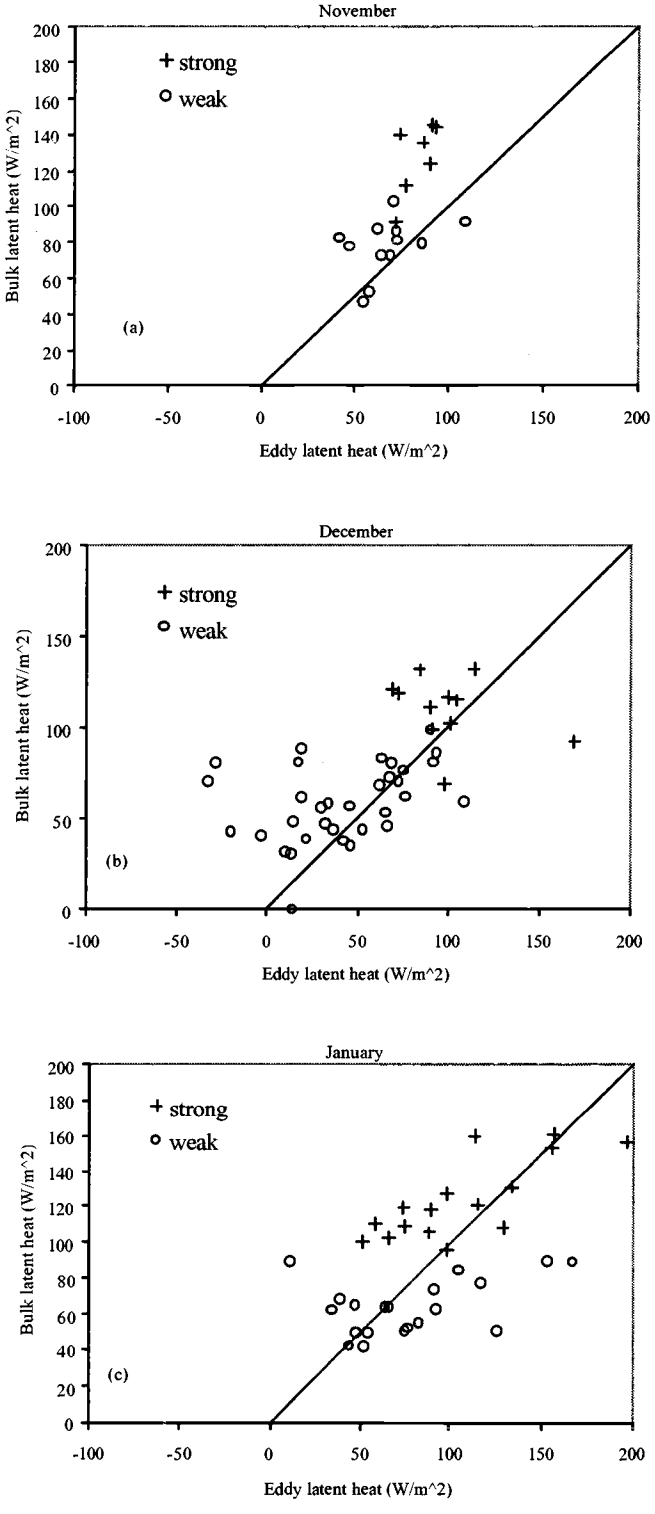

Figure 6.4: Eddy vs. bulk latent heat flux month by month

6.3.2 Sensible heat

Sensible heat estimates are compared in a similar manner in Figure 6.5. In November and December, strong wind fluxes are consistently larger than weak wind fluxes, but there is no clear separation in January. As was noted previously, as the eddy estimate becomes more negative, the bulk estimates remain near zero. As a result, the slopes of these correlations decrease from nearly 2:1 in November to 1:1 in December and January. It should also be noted that the slope falls off in December and January at lower levels of flux (less than 5 W/m^2); again, this is consistent with the discrepancy between the bulk and eddy estimates in cases of downward heat flux. In January, the only month during which there are sufficient flight legs for this comparison, the error between bulk and eddy at low levels of flux is greater in the strong wind cases.

There is a bias in all months towards the bulk estimate. As was noted with latent heat, scatter in these correlations is high (50% of the range of eddy fluxes) indicating that, on a leg-by-leg basis, the bulk method is not a strong predictor of eddy correlation flux. This prediction can, however, be improved (with some offset) as more legs are averaged.

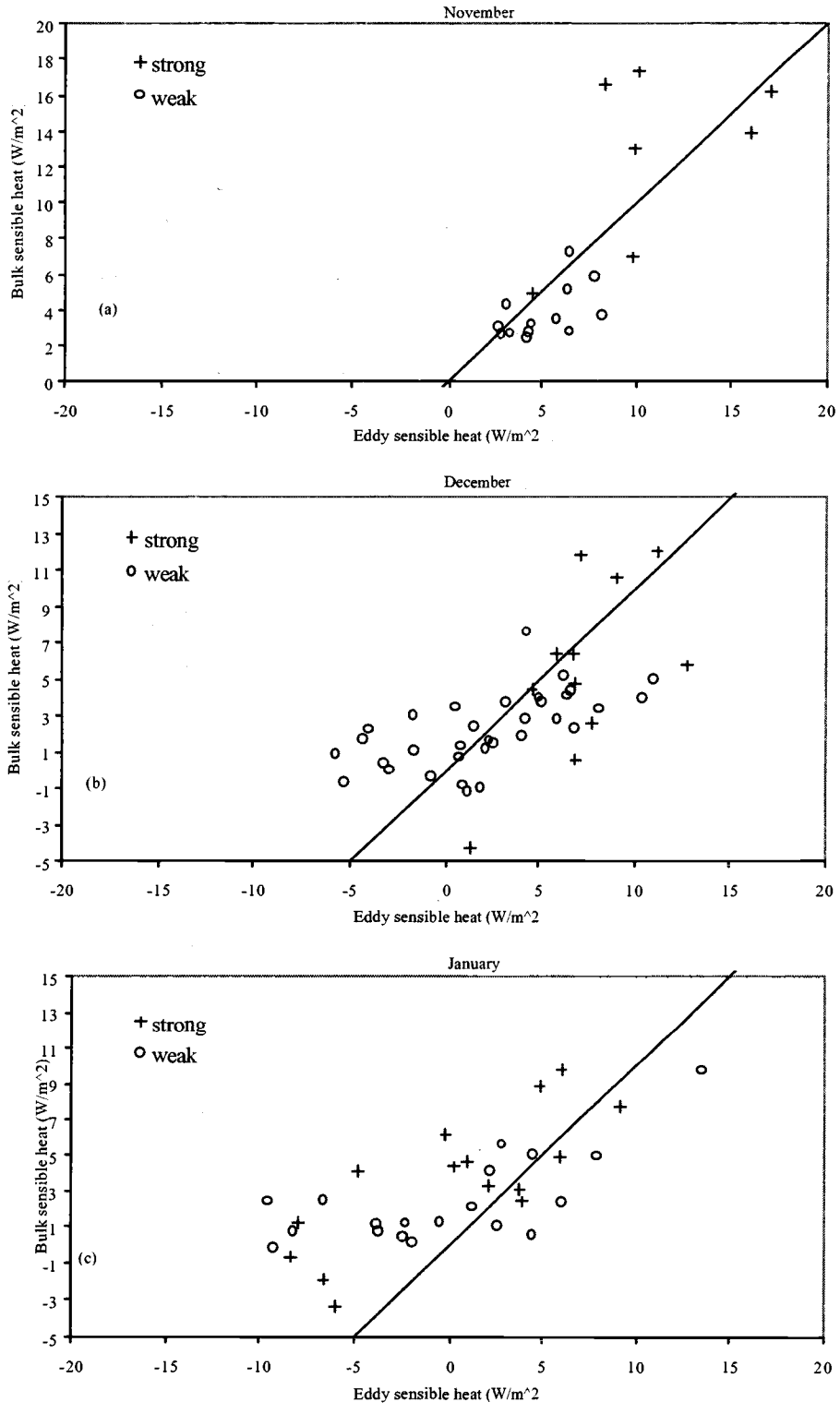

Figure 6.5: Eddy vs. bulk sensible heat flux month by month

7. Conclusion and Discussion

The differences between eddy and bulk estimates of surface heat flux as measured from the NCAR Electra during TOGA COARE have been discussed at length. Two techniques for calibration of fast response humidity sensors have been presented. An analysis has been completed to determine the proper averaging length scale to include most of the turbulent heat flux while excluding mesoscale motions. An overview of the bulk aerodynamic method used in TOGA COARE (i.e., the COARE algorithm) has also been presented. The contribution of mesoscale motion to the bulk estimate has been assessed as well.

Through all of this analysis, two statements stand clear. First, the bulk aerodynamic method, using the COARE algorithm, consistently overpredicts the eddy correlation flux for flights made by the Electra during TOGA COARE. And second, mesoscale enhancement of heat flux is greatest in light winds.

In discussing fast-response humidity measurement, two data calibration schemes were compared, a loose-couple method developed by NCAR and the in-field calibration method proposed by Friehe et al (1986). The method chosen for use in this study was the loose-couple method because of its applicability to a large range of operating conditions, its use of a laboratory standard for calibration, and the check for data quality (i.e., discontinuities) inherent in the NCAR method. It was shown that, as a result of this choice of calibration, eddy correlation latent heat fluxes would tend to be lower than those computed with data calibrated using the method of Friehe et al (1986) by up to 10%. Errors between the bulk latent heat flux estimate and the eddy correlation latent heat flux were shown to be less than 5% in the surface layer. Use of the Friehe et al (1986) method would have significantly increased the discrepancy between the bulk and eddy correlation latent heat fluxes.

Over-prediction of the bulk fluxes occurs with averaging lengths of 2 to 3 km and is significant even with gustiness correction. This bias is seen down to altitudes of 50m and increases with altitude. Some of the error may be attributed to errors in the sea-surface temperature measurement (it accounts for about 20% of the bias in the sensible heat flux) and limitations of the validity of the Monin-Obhukov similarity relationships outside of the surface layer. In light of this, it may be useful to revisit the heat flux during TOGA COARE using the most current corrections for sea-surface temperature measured from the Electra. Finally, there is work to be done in determining what, if any, other corrections may be made to the algorithm to improve its accuracy in buoyancy-driven cases. For example, in the formulation for roughness length, the smooth flow assumption could be improved by incorporating the effects of gustiness and wave age.

Esbensen & McPhaden (1996) have previously documented the effect of mesoscale enhancement in light winds. This work confirms that conclusion and shows that it may be applied to flights at various altitudes. There could, however, be further study to determine the dependence of mesoscale enhancement on averaging length, and therefore grid box size. The correlations between sensible and latent heat estimates discussed in this paper are interesting, although possibly spurious. If sensible heat and latent heat are not independent as defined within this paper and previously shown in research on the Bowen ratio, it would be useful to explore ways to further separate the two. In this light, further work to determine the interdependence of sensible and latent heat flux may be of interest.

References

Blanc, T.V., 1987: Accuracy of bulk-method determined flux, stability, and sea surface roughness. *Journal of Geophysical Research*, **92**, 3867-3876.

Bradley, E.F., P.A. Coppin, and J.S. Godfrey, 1991: Measurements of sensible and latent heat flux in the western equatorial Pacific Ocean. *Journal of Geophysical Research*, **96**, 3375-3389.

Burns, S.P., D. Khelif, C.A. Friehe, P. Hignett, A.G. Williams, A.L.M. Grant, J.M. Hacker, D.E. Hagan, Y.L. Serra, D.P. Rogers, E.F. Bradley, R.A. Weller, C.W. Fairall, S.P. Anderson, C.A. Paulson, and P.A. Coppin, 2000: Comparisons of aircraft, ship, and buoy radiation and SST measurements from TOGA COARE. *Journal of Geophysical Research*, **105**, 15,627-15,652.

_____, D. Khelif, C.A. Friehe, A.G. Williams, P. Hignett, A.L.M. Grant, J.M. Hacker, D.P. Rogers, E.F. Bradley, R.A. Weller, M.F. Cronin, S.P. Anderson, C.W. Fairall, and C.A. Paulson, 1999: Comparisons of aircraft, ship, and buoy meteorological measurements from TOGA COARE. *Journal of Geophysical Research*, **104** , 30,853-30,884.

Chang, H. and R.L. Grossman, 1999: Evaluation of bulk flux algorithms for light wind conditions using data from the Coupled Ocean-Atmosphere Response Experiment (COARE). *Quarterly Journal of the Royal Meteorological Society*, **125**, 1551-1587.

Charnock, H., 1955: Wind stress on a water surface. *Quarterly Journal of the Royal Meteorological Society*, **81**, 639-640.

Chou, S., Wenzhong W., M. Chou, 2000: Surface Heat Budgets and Sea Surface Temperature in the Pacific Warm Pool during TOGA COARE. *Journal of Climate*: **13**, 634–649.

Esbensen, S.K. and Y. Kushnir, 1981: The heat budget of th eglobal ocean: An atlas based on estimates from surface marine observations. Climactic Research Institute Report No. 29, Oregon State University, Corvallis, Oregon, 27 pp.

_____ and R. W. Reynolds, 1991: Estimating monthly averaged air-sea transfers of heat and momentum using the bulk aerodynamic method. *Journal of Physical Oceanography*, **11**, 457-465.

_____ and M.J. McPhaden, 1996: Enhancement of tropical ocean evaporation and sensible heat flux by atmospheric mesoscale systems. *Journal of Climate*, **9**, 2307-2325.

Fairall, C.W., E.F. Bradley, D.P. Rogers, J.B. Edson, and G.S. Young, 1996: Bulk parameterization of air-sea fluxes for a Tropical Ocean Global Atmosphere Coupled Ocean-Atmosphere Response Experiment. . *Journal of Geophysical Research*, **101**, 3747-3767.

Friehe, C.A., R.L. Grossman, and Y. Pann, 1986: Calibration of an airborne Lyman-alpha Hygrometer and Measurement or Water Vapor Flux Using a Thermoelectric Hygrometer. *Journal of Oceanic and Atmospheric Technology*, **3**, 299-304.

_____, W.J. Shaw, D.P. Rogers, K.L. Davidson, W.G. Large, S.A. Stage, G.H. Crescenti, S.J.S. Khalsa, G.K. Greenhut, and F. Li, 1991: Air-sea fluxes and surface layer turbulence around a sea surface temperature front. *Journal of Geophysical Research*, **96**, 8593-8609.

Garratt, J. R., 1977: Review of drag coefficients over oceans and continents. *Monthly Weather Review*, **105**, 915-929.

_____, 1992: : *The Atmospheric Boundary Layer.* Cambridge University Press. 316 pp.

Godfrey, J. S. and A.C.M. Beljaars, 1991: On the turbulent fluxes of buoyancy, heat and moisture at the air-sea interface at low wind speed. *Journal of Geophysical Research*, **96**, 22043-22048.

_____, R.A. Houze, Jr., R.H. Johnson, R. Lukas, J.L. Redelsperger, A. Sumi, and R. Weller, 1998: Coupled Ocean-Atmosphere Response Experiment (COARE): An interim report. *Journal of Geophysical Research*, **103**, 14395-14450.

Grachev, A.A., C.W. Fairall, S.E. Larsen, 1998: On the determination of the neutral drag coefficient in the convective boundary layer. *Boundary Layer Meteorology*, **86**, 257-278.

Grant A.L.M. and P. Hignett, 1998: Aircraft observations of the surface energy balance in TOGA-COARE. *Quarterly Journal of the Royal Meteorological Society*, **124**, 101-122

Greenhut, G.K. and S.J.S. Khalsa, 1995: Bulk transfer coefficients and dissipation-derived fluxes in low wind speed conditions over the western equatorial Pacific Ocean. *Journal of Geophysical Research*, **100**, 857-863.

Greischar, L. and R.B. Stull, 1999: Convective transport theory for surface fluxes, tested over the western Pacific warm pool. *Journal of the Atmospheric Sciences*, **56**, 2201-2211.

Hagan, D., D. Rogers, C. Friehe, R. Weller, and E. Walsh, 1997: Aircraft Observations of Sea Surface Temperature Variability in the Tropical Pacific. *Journal of Geophysical Research*, **104**, 30,853-30,883.

Hasse, L. and S.D. Smith, 1997: Local sea surface wind, wind stress, and sensible and latent heat fluxes. *Journal of Climate*, **10**, 2711-2724.

Howell, J. and L. Mahrt, 1997: Multiresolution Flux Decomposition. *Boundary Layer Meteorology*, **83**, 117-137

Howell, J., 1995: Identifying sudden changes in data. *Monthly Weather Review*, **123**, 1207-1212.

Jabouille, P., J. L. Redelsperger, and J. P.Lafor, 1996: Modification of Surface Fluxes by Atmospheric Convection in the TOGA COARE Region. *Monthly Weather Review*, **124**, 816-837.

Johnson, R.H and M.E. Nicholls, 1983: A composite analysis of surface heat flux. *Monthly Weather Review*, **111**, 308-319.

Kara, A.B., P.A. Rochford, and H.E. Hurlburt, 2000: Efficient and Accurate Bulk Parameterizations of Air-Sea Fluxes for Use in General Circulation Models. *Journal of Oceanic and Atmospheric Technology*, **17**, 1421-1438.

Khelif, D., C. A. Friehe and S. P. Burns, 1997: Boundary-Layer and Turbulent Flux Measurements From the TOGA COARE Aircraft, 22nd Conference on Hurricanes & Tropical Meteorology, American Meteorological Society, 254-255.

Ledvina, D.V., G.S. Young, R.A. Miller, and C.W. Fairall, 1993: The effect of averaging on bulk estimates of heat and momentum fluxes for the tropical western Pacific Ocean. *Journal of Geophysical Research*, **97**, 20,211-20,217.

Lenschow, D.H, J. Mann, and L. Kristensen, 1994: How long is long enough when measuring fluxes and other turbulence statistics? *Journal of Atmospheric and Oceanic Technology*, **11**, 661-673.

Liu, W. T., K. B. Katsaros and J. A. Businger, 1979: Bulk parameterization of the air-sea exchange of heat and water vapor including the molecular constraints at the surface. *Journal of the Atmospheric Sciences*, **36**, 1722-1735.

Lobocki, L., 2001: Calculation of Surface Fluxes Under Convective Conditions by Turbulence Closure Models. *Journal of Applied Meteorology*, **40**, 604-621.

Lyman-Alpha Data Processing Technique (Standard RAF Processing), 1992: National Center for Atmospheric Research.

Mahrt, L., 1987: Grid-averaged surface fluxes. *Monthly Weather Review*, **115**, 1550-1560.

_____ and J. Sun, 1995: Dependence of surface exchange coefficients on averaging scale and grid size. *Quarterly Journal of the Royal Meteorological Society*, **121**, 1835-1852.

_____, D. Vickers, J. Howell, J. Hojstrup, J.M. Wilczak, J. Edson, and J. Hare, 1996: Sea surface drag coefficients in the Riso Air Sea Experiment. *Journal of Geophysical Research*, **101**, 14327-14335.

Panofsky H.A. and J.A. Dutton, 1984: *Atmospheric turbulence, models and method for engineering applications*, John Wiley and Sons, 397 pp.

RAF Bulletin No. 22, 1987. Airborne Humidity Measurements. National Center for Atmospheric Research, 7pp.

Redelsperger J.L., F. Guichard, and S. Mondon, 2000: A Parameterization of Mesoscale Enhancement of Surface Fluxes for Large-Scale Models, *Journal of Climate*, **13**, 402-421.

Rogers, D. P., D.W. Johnson, and C. A. Friehe, 1995: The Stable Internal Boundary Layer Over a Coastal Sea Part I: Airborne Measurements of the Mean and Turbulence Structure. *Journal of the Atmospheric Sciences*, **52**, 667-683.

Saxen, T., and S. A. Rutledge, 1998: Surface fluxes and boundary layer organization in TOGA COARE: Sensitivity to convective organization. *Journal of the Atmospheric Sciences*, **55**, 2763-2781.

Schanot, A.J., 1987: Evaluation of the Uses and Limitations of Lyman-alpha Hygrometer as an Operational Airborne Humidity Sensor. *Preprints, Sixth Symposium on Meteorological Observations and Instrumentation*, New Orleans, LA, American Meteorological Society, 257-260.

_____ and P. Spyers-Duran, 1987: Airborne Intercomparison of Three Hygrometers. *Preprints, Sixth Symposium on Meteorological Observations and Instrumentation*, New Orleans, LA, American Meteorological Society, 209-212.

Smith, S. D., 1988: Coefficients for sea surface wind stress, heat flux, and wind profiles as a function of wind speed and temperature. *Journal of Geophysical Research*, **93**, 15467-15472.

Song, X., Friehe, C.A. and D. Hu, 1996: Ship-board Measurements and Estimations of Air-Sea Fluxes in the Western Tropical Pacific Ocean. *Boundary-Layer Meteorology*.

Stull, R.B., 1988: *An Introduction to Boundary Layer Meteorology.* Kluwer Academic. 666 pp.

Sun, J., S.K. Esbensen, and L. Mahrt, 1995: Estimation of surface heat flux. *Journal of the Atmospheric Sciences,* **52**, 3162-3171.

_____, and L. Mahrt, 1995: Determination of surface fluxes from the surface radiative temperature. *Journal of the Atmospheric Sciences*, **52**, 1095-1106.

_____, L. Mahrt, J.F. Howell, S.K. Esbensen, L. Mahrt, C. Greb, R. Grossman, and M.A. LeMone, 1996: Scale dependence of air-sea fluxes over the Western Equatorial Pacific. *Journal of the Atmospheric Sciences*, **53**, 2997-3012.

Vickers, D. and S.K. Esbensen, 1998: Subgrid surface fluxes in fair weather conditions during TOGACOARE: Observational estimates and parameterization. *Monthly Weather Review,* **126**, 620-633.

_____ and L. Mahrt, 1997a: Fetch limited drag coefficients. *Boundary Layer Meteorology,* **85**, 53-79.

_____ and L. Mahrt, 1997b: Quality control and flux sampling problems for tower and aircraft data. *Journal Atmospheric And Oceanic Technology,* **14**, 512-526.

Webb, E. K., G. I. Pearman, and R. Leuning, 1980: Correction of flux measurements for density effects due to heat and water vapor transport. *Quarterly Journal of the Royal Meteorological Society,* **106**, 85-100.

Webster, P.J., and R. Lucas, 1992: TOGA COARE: The Coupled Ocean-Atmosphere Response Experiment. *Bulletin of the American Meteorological Society,* **73**, 1377-1416.

Williams, A.G., 2001: A physically based parameterization for surface flux enhancement by gustiness effects in dry and precipitating convection.. *Quarterly Journal of the Royal Meteorological Society,* **127**, 469-491.

_____ and J.M. Hacker, 1995: Multiscale Aircraft Flux Measurements in the TOGA COARE Boundary Layer. *Proceedings of the International Scientific Conference on Tropical Ocean Global Atmosphere (TOGA) Programme*, Melbourne, Australia, World Meterological Organization, 444-448.

_____, Kraus, H., Hacker, J.M., 1996: Transport Processes in the Tropical Warm Pool Boundary Layer, Part I: Spectral Composition of Fluxes. *Journal of the Atmospheric Sciences,* **53**, 1187-1202

World Meteorological Organization, 1985: Scientific Plan for the Tropical Ocean and Global Atmosphere Proramme. WCRP Publications, Series No. 3, WMO/TD 64, Geneva.

Young, G.S., D.V. Ledvina, and C.W. Fairall, 1992: Influence of precipitating convection on the surface energy budget observed during a Tropical Ocean Global Atmosphere pilot cruise in the tropical western Pacific ocean. *Journal of Geophysical Research*, **97**, 9595-9603.

Zeng, X., M. Zhao, and R.E. Dickinson, 1998: Intercomparison of bulk aerodynamic algorithms for the computation of sea surface fluxes using the TOGA COARE and TAO data. *Journal of Climate*, **11**, 2628-2644.